FIRST-PRINCIPLES INVESTIGATION OF STRUCTURAL DEFECTS AND ENERGY LANDSCAPE AFFECTING DIFFUSION IN Cr_2O_3 AND Al_2O_3

by

Corinne Gray

B.S Physics, University of California at Merced, 2012

Submitted to the Graduate Faculty of

Swanson School of Engineering in partial fulfillment

of the requirements for the degree of

Doctor of Philosophy

University of Pittsburgh

2017

UNIVERSITY OF PITTSBURGH

SWANSON SCHOOL OF ENGINEERING

This dissertation was presented

by

Corinne Gray

It was defended on

March 29, 2017

and approved by

Brian Gleeson, PhD, Harry S. Tack Chair Professor and Department Chair,

Mechanical Engineering and Materials Science

Tevis Jacobs, PhD, Assistant Professor,

Mechanical Engineering and Materials Science

John Keith, PhD, Inaugural Richard King Mellon Faculty Fellow in Energy,

Chemical and Petroleum Engineering

Dissertation Director: Guofeng Wang, PhD, Associate Professor,

Mechanical Engineering and Materials Science

FIRST-PRINCIPLES INVESTIGATION OF STRUCTURAL DEFECTS AND ENERGY LANDSCAPE AFFECTING DIFUSION IN Cr_2O_3 AND Al_2O_3

Corinne Gray, PhD

University of Pittsburgh, 2017

In this study, chromia vacancy diffusion and alumina grain boundary structure have been investigated using the first principles density functional theory (DFT) computational methods. Comparing the predictions from the DFT and DFT+U methods on chromia, it was found that the DFT+U method describes α-Cr_2O_3 crystal better in terms of the magnetism, band gap, charge state of vacancies, and migration energies for charged vacancy diffusion than the DFT method. For Cr_2O_3, four distinct elementary diffusion paths were investigated for Cr and O vacancies, both with and without charge. For charged vacancies our DFT+U calculation predicted that the energy barrier for V_{O}^{2+} diffusion varies from 1.18 to 2.98 eV and for V_{Cr}^{3-} diffusion varies from 2.02 to 2.59 eV. In comparison, the same diffusion paths had migration energy differences as high as 1.19 eV (for $O_1 \rightarrow O_3$) and 0.99 eV for ($Cr_1 \rightarrow Cr_3$) when examining the neutral vacancies. These changes in migration energies indicates charge state of defects plays an important role in determining the diffusion properties through an oxide. For alumina, the fully relaxed structures of $\Sigma 11\{10\bar{1}1\}/\{10\overline{\bar{1}1}\}$ grain boundary doped with one Y, one Hf, or two Hf atoms within the grain boundary have been investigated in detail. It was found that the introduction of reactive element

dopants results in pinning, reducing diffusion through the grain boundary. Specifically, pinning was more strongly observed for Hf than Y. As compared to the replaced Al, Hf and Y dopants were found to change the local charge density, and introduce some defect states within the band gap. Low concentration of Hf and Y dopants causes an increase in the number of defects states near the valence band maximum, implicating an increase of hole diffusion. In contrast, increasing the concentration of Hf dopants was found to reduce the number of defect states, suggesting an effect to slow diffusion in the alumina grain boundary.

TABLE OF CONTENTS

LIST OF TABLES

LIST OF FIGURES

LIST OF EQUATIONS

PREFACE

I would like to thank my family and friends for their constant encouragement and support during my time here at the University of Pittsburgh, without you I could not have finished my doctorate and for that I thank you.

Corinne

1.0 INTRODUCTION

Oxide coatings can be found easily in nature, as most metals (all non-noble metals) when exposed to oxygen will undergo a chemical reaction forming a metal-oxide. Due to their common occurrence, oxides have been used in many applications, such as catalyst, abrasives, semiconductors, glass, filters, and protective layers. In particular their use as high temperature diffusion barrier coatings has been of interest due to their wide application in aviation (airplane turbine blades), automotive systems (exhaust), industry (catalyst), and energy production (nuclear reactors). This work will focus on two types of oxides, chromium (III) oxide and aluminum (III) oxide which are introduced in more detail below.

Chromium (III) oxide (also known as chromia) is an inorganic compound with the chemical formula Cr_2O_3. It possesses a high melting temperature (~2300°C), high hardness (37 ± 4 GPa in bulk), high wear resistance, high temperature oxidation resistance, and low friction coefficient [1, 2]. Hence, Cr_2O_3 has been employed in various applications such as metal-oxide semiconductors, fuel cell electrodes, gas sensors, heterogeneous catalyst, and thermal barrier coatings [3]. Particularly of interest is the oxide scale formation of α-Cr_2O_3 on high temperature alloys, such as stainless steels.

Aluminum (III) oxide (alumina) is a lightweight ceramic with the chemical formula Al_2O_3, possessing a high hardness (38.4 ± 5.5 GPa) [4], high melting point (2051°C) [5], strength, chemical stability, and wear resistance. Thus, it has been used as a catalyst, filter, abrasive, and

abrasion protective coat. Like chromia, alumina is also commonly used as a protective oxide however, on nickel based superalloys.

Due to the common use of alumina and chromia as high temperature oxide layers, there have been vast amounts of studies on diffusion and the effect of point defects through the systems. To fully understand the relation between the growth of protective scales and point defects in metal oxides, first-principles density functional theory (DFT) simulations have been performed complementary to experimental measurements. These simulations are believed to be a useful approach by predicting the migration energies of individual species in oxides at an atomistic scale [6, 7], in both the bulk and grain boundary.

1.1 POINT DEFECTS

Most systems contain small amounts of crystallographic defects in the atomic structure, these can contain point defects, line defects, planar defects, or bulk defects. In this study, we will focus on point defects, in particular: vacancies, substitution impurities, and interstitial atoms. To define our vacancies the Kröger-Vick notation is used, which follows the scheme M_S^C, where *M* is the species (metal atom or vacancy), *C* is the charge (• for positive, ‘ for negative, and ^{x} for neutral charge), and *S* is the lattice location [8].

Vacancies are defined as an unoccupied atomic position that is normally occupied in the perfect crystal [8]. A vacancy does not mean the atom has been completely removed from the system. It can be repositioned to another position in the crystal, such as an interstitial position or in a grain boundary. When an atom is displaced to an interstitial position and thus creates a vacancy, it is called a Frenkel defect [8]. For example, in chromia a Frenkel defect can be

V_{Cr}^{3-} and Cr_i^{3+} which form the Frenkel pair. If a series of vacancies accumulates to form charge-compensating anion and cation vacancies, they form a Schottky defect [8]. An example for chromia would be three oxygen vacancies (V_O^{2-}) and two chromia vacancies (V_{Cr}^{3+}), to ensure the net charge remains neutral.

Interstitial atoms occur when an atom or ion, of the same species as the material, is in a site where an atom is not normally located [8]. In the case of chromia, an example would be a chromium atom placed in a location where there is neither chromium nor oxygen atoms. Substitutional impurities, which can be introduced by doping, are when an atom/ion of a different type replaces one of the host atoms/ions [8]. In the case of alumina, an example can be replacing an aluminum atom with another metal atom such as yttrium or hafnium.

1.2 CHROMIA DIFFUSION

Formation of thermally-grown α-Cr_2O_3 scale on high temperature alloys, such as stainless steels, provides protection to the underneath alloys from extensive oxidation corrosion. In this case, inward diffusion of oxygen and/or outward diffusion of metals will lead to the continuous thickening of the chromia scale. As the thickness increases, the probability of spalling and cracking in the protective scale also increases. These diffusion-induced mechanical failures of α-Cr_2O_3 scale could result in undesired, further oxidation of the alloys [9].

Consequently, many studies have been carried out to quantify and elaborate the diffusion processes through chromia scales. Measuring the simultaneous diffusion of ^{18}O and ^{54}Cr in Cr_2O_3 scales using Secondary Ion Mass Spectrometry (SIMS), Tsai *et al.* found that the Cr_2O_3 scale

growth proceeded with a counter-current diffusion of O and Cr ions mainly through grain boundaries [10, 11]. They also found that the grain boundary diffusion coefficients of O and Cr were about five orders of magnitude higher than the lattice diffusion coefficients of O and Cr for Cr_2O_3 scales formed on a $Ni_{70}Cr_{30}$ alloy at temperature of 900 ºC and oxygen partial pressure of 0.1 atm [10, 12]. Comparing the oxidation constants of chromia-forming alloys and the measured self-diffusion coefficients of O and Cr in Cr_2O_3, Sabioni *et al.* showed that even the fast grain-boundary diffusion of oxygen was not able to explain the observed high growth rate of Cr_2O_3 scales and hence suggested that other short-circuit diffusion (such as microcracks, porosities, or channels) might be responsible for the growth of Cr_2O_3 scales [13].

To gain mechanistic insight into the relation between the growth of protective scales and diffusion processes in metal oxides, the first-principles density functional theory (DFT) computation method (complementary to experimental measurements) can be used to predict the migration energies of individual charged species in oxides at an atomistic scale [14, 15]. In this contribution, we employed the DFT calculation methods to study the vacancy diffusion in bulk Cr_2O_3 crystal lattice. Although lattice diffusion is not regarded as a predominant process during the growth of Cr_2O_3 scales, computational study of lattice diffusion is an essential first step to validate the computation methods against available experimental data [10, 13] and thus paves the road for future study of other complex short-circuit diffusion processes in Cr_2O_3 scales.

To date, there have been two DFT studies on the lattice diffusion through ion-vacancy exchange mechanism in Cr_2O_3 crystal. Yu *et al.* used the DFT method as implemented in CASTEP code and predicted that the diffusion of O^{2-} and Cr^{3+} to their nearest neighboring lattice sites of Cr_2O_3 crystal required a migration energy of 1.15 eV and 2.02 eV, respectively [16]. It should be pointed out that a long-range diffusion in Cr_2O_3 crystal cannot be constituted only by these

shortest-distance diffusion paths. Namely, there exist multiple elementary diffusive paths in the Cr_2O_3 crystal. Recognizing this point, Lebreau *et al.* investigated the diffusion of O^{2-} and Cr^{3+} vacancies along various diffusion paths in Cr_2O_3 crystal using the DFT+U computational method implemented in VASP [17]. They predicted that the migration energy of O^{2-} ranged between 2.21 eV to 3.65 eV whereas the migration energy of Cr^{3+} varied between 2.57 eV to 3.21 eV. We noticed that Lebreau *et al.* still missed one low-energy elementary diffusive path, respectively, for O^{2-} and Cr^{3+} lattice diffusion in Ref. 17.

In this study, we present our first-principles calculation results for a set of four low-energy paths for charged O and Cr vacancy diffusion in α-Cr_2O_3 bulk crystal, respectively. These results are critical inputs of the kinetic Monte Carlo method for prediction of lattice diffusion constants in Cr_2O_3. Moreover, the two prior calculations [16, 17] gave predictions differing by 1.06 eV for the same shortest-distance diffusion path of O^{2-}. This discrepancy in the theoretical results demands a careful examination of the prediction uncertainties associated with the different DFT methods employed. In this regard, we performed both the DFT and DFT+U calculations for the lattice diffusion of O and Cr ions in Cr_2O_3 and benchmarked the predictions from the two DFT methods against available experimental data in this work. In this way, we identify the computational approach necessary for accurate prediction of diffusion in α-Cr_2O_3 scales.

1.3 DIFFUSION THEORIES

Recently the model of diffusion for Al_2O_3 has been brought up for debate. Reactive elements (REs) have been shown to reduce the scale growth rate [18], However, how this is accomplished is still not well understood. Point defect jumping has been the primary theory for diffusion in alumina

grain boundaries. In the grain boundary, REs are believed to physically block diffusion (site-blocking) or slowing diffusion via electronic effects (swamping out) [19]. However, there are fundamental problems with site-blocking and point defect jumping. For example, if REs block point defect jumping due to size, then Y would slow grain boundary diffusion more than Hf. This is however not the case [20, 21]. Heuer states there are two problems with point defect jumping as the primary mechanism for Al_2O_3 grain boundary diffusion. One is the diffusion coefficients for grain boundaries and short-circuit diffusion, which are comparable in value although grain boundaries should have a lower activation energy due to their geometry (more space to allow for quicker jumping). Second, the ability of the grain boundary "to transform point defects into delocalized atomic rearrangements renders the very idea of point defects at grain boundaries problematic" [22]. It then becomes important to fully understand the structure and properties of the grain boundary to begin exploring new theories of diffusion.

1.4 ALUMINA GRAIN BOUNDARY

Alumina is commonly observed as a protective coating at high temperature applications on alloys such as Fe-Ni-Cr superalloys, some ferratic stainless steels, and Co based superalloys [23]. As a protective coating, it is key to ensure the scale does not grow too thick as spalling may occur, resulting in an exposure to the underlying structural material. It is believed that in alumina scales, transport is predominantly controlled by inward oxygen diffusion through the grain boundary, however the outward aluminum diffusion via grain boundaries cannot be ignored [24]. It is then important to study how structure and electronic properties can affect grain boundary diffusion.

In polycrystalline samples, low angle grain boundaries (<5°) represent a small percentage of the total number of grains, less than 4% per Cho *et al.* [25]. Experimentally, high angel grain boundaries such as $\Sigma7[2\bar{1}\bar{1}0]$, $\Sigma11[2\bar{1}\bar{1}0]$, $\Sigma13[2\bar{1}\bar{1}0]$, $\Sigma19[2\bar{1}\bar{1}0]$, $\Sigma11[01\bar{1}0]$, $\Sigma13[01\bar{1}0]$, $\Sigma23[01\bar{1}0]$, *and* $\Sigma31[01\bar{1}0]$ have been observed by Cho *et al.* in polycrystalline samples. So far, the structures of several types of alumina grain boundaries have been studied in an atomic scale using high-resolution transmission electron microscopy (HRTEM) technique. Most often, these grain boundaries were constructed using the bicrystal method, in which "a sample containing two grains with the required orientation of the planar separating interface" is used [26].

Using these techniques, Nakagawa *et al.* examined five undoped alumina grain boundaries, $\Sigma7\{2\bar{3}10\}$, $\Sigma7\{4\bar{5}10\}$, $\Sigma21\{2\bar{3}10\}$, $\Sigma21\{4\bar{5}10\}$, and $\Sigma31\{7\bar{1}\bar{1}40\}$ [51] and the $\Sigma31\{7\bar{1}\bar{1}40\}$ grain boundary doped with Y [19]. For undoped alumina grain boundaries they found the oxygen diffusion could differ by up to three orders of magnitude depending on the grain boundary's character [27], and when adding Y the oxygen diffusion was slowed (>10 times) in the temperature range of 1400-1600°C [19]. Gemming *et al.* have studied $\Sigma3\{10\bar{1}0\}$, $\Sigma7\{10\bar{1}2\}$, $\Sigma11\{20\bar{2}2\}$, $\Sigma13\{21\bar{1}3\}$, and $\Sigma23\{\bar{2}114\}$ alumina grain boundaries and found that the grain boundary geometry determines the amount of impurities it contains not the gradients due to the processing conditions [28]. Near Σ3 <0001> and low angle (~Σ1) tilt grain boundaries were also examined with respect to dislocation, and found the stacking fault length decreased with increasing misorientation angle [29]. Nishimura *et al.* examined various Σ7 tilt grain boundaries ($\Sigma7\{1\bar{1}02\}, \Sigma7\{2\bar{3}10\}, \Sigma7\{4\bar{5}10\}$), and found that although the Σ-values were the same for all three grain boundaries, the grain boundary energies (measured via a thermal grooving technique) were found to differ (0.44, 3.99, and 3.9 J/m^2 respectively) [30].

Complementary to aforementioned experimental studies, the first-principles computational methods have been used to study the geometric and electronic structures of alumina grain boundaries. The basal (Σ3) twin was examined with mirror, twofold-rotation, and glide-mirror symmetries were examined using LDFT (local-density functional theory) and empirical shell-model potentials and found the rotation twin to have the lowest energy using both methods [31]. Lei performed DFT grain boundary simulations on Σ3(0001) and $\Sigma 3(10\bar{1}0)$ (using the model created by Fabris *et al.* [32]) and found that the activation energies were higher than bulk for $\Sigma 3(10\bar{1}0)$ and lower for Σ3(0001) for both oxygen and aluminum [14]. Guhl *et al.* performed DFT simulations on $\Sigma 7\{4\bar{5}10\}[0001]$ and $\Sigma 7\{2\bar{3}10\}[0001]$ grain boundaries finding the later to be wider, suggesting more rapid diffusion [33]. Fabris and Elsässer used LDFT simulations on $\Sigma 13(10\overline{14})$ mirror twin boundary found three stable configurations, one aluminum terminated and two oxygen terminated boundaries finding the Al terminated surface to have lower energy [34]. Fabris and Elsässer also explored, again using LDFT, the electronic properties of $\Sigma 3(10\bar{1}0)$, $\Sigma 7(10\bar{1}2)$, and $\Sigma 13(10\bar{1}4)$, further exploring concentration effects of Y on the grains at both ~3 and 6 atoms/nm^2 finding the change in the electronic structure to be strongly localized around the first neighboring shell of oxygen atoms [35].

Heuer and colleagues have performed various theoretical and experimental works on alumina, exploring the electronic properties and its effect on diffusion. A density functional theory (DFT) and experimental work was performed on an undoped $\Sigma 7\{4\bar{5}10\}$ grain boundary, and found the electrons and holes play a large role in the growth of alumina [22]. Further DFT results on $\Sigma 7\{4\bar{5}10\}[0001]$ and $\Sigma 7\{4\bar{3}10\}[0001]$ found that localized states above the valence band maximum alter the accessibility of electrons and holes, and thus improve the performance of alumina [33].

Al_2O_3 is commonly doped to improve physical qualities, as well as decrease diffusion rates. Reactive elements (REs) such as Y [19, 20, 36], Zr [17], Hf [20, 38], La [36], and Lu [36], have been shown to increase creep resistance, enhance scale adhesion, changing the scale growth mechanism slow grain boundary diffusion, and decrease void formation at the scale/alloy interface in alumina [18]. For example, Chen *et al*. computationally showed Y on the Σ3 grain boundary and found a change in maximum stress from 31 (undoped) to 39 GPa (Y doped) [39].

How REs alter the properties of a grain boundary diffusion and behavior is still widely debated, is the effect physical (size) or is it electronic (bonding energy, repulsion) that results in the changed behavior. REs have been shown to diffuse to the grain boundary by both experiment and theoretical studies [20, 38, 40]. It is commonly believed that REs on the grain boundary slow grain boundary diffusion by site blocking [19, 38, 40, 42], as it is assumed that grain boundary diffusion proceeds via point defect jumping [22]. Another mechanism REs are thought to slow down diffusion in the grain boundary is "swamping out", where the RE suppresses the segregation of other cations [19].

Specifically, we conducted computational study on $\Sigma 11[2\bar{1}\bar{1}0]$ tilt grain boundary of alumina in this work. Regarding this grain boundary, Höche and Kenway created experimental and theoretical studies on $\Sigma 11[2\bar{1}\bar{1}0]$ tilt grain boundary, with the experimental work acting as the basis for creating the theoretical structure [43]. Using this model, Kenway performed simulations exploring the stacking faults in $\Sigma 11\{10\bar{1}1\}/\{10\bar{1}\bar{1}\}$ finding atoms in the grain prefer to be near unlike atoms [44]. Müllejans and French found that the Σ11 grain boundary increases the oxygen 2p valance band in comparison to bulk alumina, resulting in more ionic bonding [45]. Complementary theoretical work using orthogonalized linear combination of atomic orbital (OLCAO) method, found atoms in the grain boundary do not introduce deep states in the band

gap, finding states at the valence and conduction band edges [46]. Heuer *et al.* showed that upon adding Y to the grain boundary, the counter-flow of electrons/holes is restricted and slows down diffusion in the grain boundary [41].

Milas and Carter performed DFT calculations using the Kenway model, for an undoped and doped surface [40, 47]. In their first work, they tested the adsorption of Y, Hf, O, and Al, finding that Al, Hf, and Y prefer to adsorb to positions spatially close to each other. They also state Hf and Y should hinder the diffusion rate through the grain boundary [40]. In follow up work, they examined how Y effected translation in the a- and b-directions (they did not consider a+b translation) and found it to increase the sliding barrier [47].

In this work, we will also use the on $\Sigma 11\{10\bar{1}1\}/\{10\overline{\bar{1}1}\}$ tilt grain boundary, with Hf and Y in comparison to the undoped case. Our work is distinct from Milas and Carter, as we investigated translation in the a+b direction as well as the changes in the electronic properties due to Hf and Y.

1.5 QUESTIONS AND HYPOTHESIS

The hypothesis of this work is that diffusion, for both lattice and grain boundary, in oxide scales is influenced by electronic effects. To explore this for chromia, the charge of the vacancy will be altered and the difference in migration energies will be investigated. We turn to the density of states to explain how charge effects the behavior of defect states during the migration process. For alumina, as Y and Hf replace Al in the grain boundary the electronic properties within the grain boundary are altered, in turn influencing the behavior of grain boundary diffusion. How this is accomplished is investigated using charge density difference and the density of states. Also

investigated is how increasing the concentration of Hf in the grain boundary further influences grain boundary diffusion as the electronic properties shift even further from the undoped case.

2.0 COMPUTATIONAL METHODS

In this work, the DFT and DFT+U calculations were performed with the Vienna Ab initio Simulation Package (VASP) [52, 53]. All calculations used projector augmented wave (PAW) method [54]. Exchange correlation was treated with the generalized gradient approximation (GGA) in the form of Perdew–Burke–Ernzerhof (PBE) functional for chromia and alumina [55]. DFT (and DFT+U) parameters used for chromia and alumina are given below, in Sections 2.2.1 and 2.3.1 respectively.

2.1 THEORY OF DFT AND DFT+U

DFT gets its name by using electron density to calculate ground state energy. This is done by using the Hohenberg-Kohn-Sham Theory, which states that the ground-state energy is a unique functional of the particle density [56, 57]. To simplify equations and reduce computational cost two major approximations, the Born-Oppenheimer approximation and Hartree-Fock, are used. The Born-Oppenheimer approximation states that because the mass of a nucleus is much larger than that of the electrons, the nuclei move much slower than electrons, thus it is approximated that electrons are moving in a field of fixed nuclei [59]. The Hartree-Fock approximation is used to determine the wave function and energy state of a stationary many body quantum system by

assuming each electron can be modeled using a single Slater determinant [59, 60]. The lowest energy can then be determined as the state closest to the ground state, and thus the most stable.

DFT+U adds an additional term based on the Hubbard model for strongly interacting electron systems [61]. The +U method incorporates "orbital ordering as well as the notion that both spin and orbital polarization are driven by the screened on-site Coulomb interactions instead of the exchange interactions of the homogeneous electron gas" [61]. This means that electrons are represented more accurately when electrons are strongly coupled. The Hubbard correction is used for transition metals to better represent the d-electrons, meaning alumina does not require the +U correctional term due to aluminum being a post-transition metal. For DFT+U calculations, we used the rotationally invariant DFT+U method introduced by Liechtenstein *et al.* [61] in VASP.

2.2 METHODS USED FOR CHROMIA

2.2.1 Calculation Specifics

The physical properties of Cr_2O_3 bulk crystal were calculated using a conventional hexagonal cell of stoichiometric $Cr_{12}O_{18}$ and a 5x5x2 Monkhorst-Pack k-point mesh for k-space integration. The vacancy defects and lattice diffusions in Cr_2O_3 crystal were modelled using a 2x2x1 supercell of conventional hexagonal cells with three axes along $[2\bar{1}\bar{1}0]$ (spanning 10.1 Å), $[\bar{1}2\bar{1}0]$ (spanning 10.1 Å), and [0001] (spanning 13.9 Å) directions. The lattice diffusion calculations used a 3x3x2 Monkhorst-Pack k-point mesh whereas the density of state (DOS) of vacancies were computed using a finer 15x15x10 Monkhorst-Pack k-point mesh. Fully optimized Cr_2O_3 crystal structures and vacancy defects were obtained by reducing the Hellman-Feynman force acting on each ion to

be less than 0.01 eV/Å. For DFT+U parameters, we chose an effective on-site Coulomb interaction parameter U = 4.5 eV and exchange parameter J = 1 as suggested in Ref. [62].

2.2.2 Diffusion Calculations

For chromia diffusion calculations, the transition states of lattice diffusions were located using the climbing image nudged elastic band (CI-NEB) method [63]. In the CI-NEB method requires two fully relax endpoints then a number of 'images' (in this case 3) are relaxed simultaneously. These images are structures along a path between the two end points, in this case a Cr or O atom moving from one location to another. Force components both along and perpendicular to the tangent of the reaction path were relaxed to be less than 0.05 eV/Å. The migration energy for vacancy diffusion was then calculated as the energy difference between the transition and initial states during a diffusive jump of exchanging of a (Cr or O) atom with a neighboring vacancy.

2.2.3 Charged Vacancy Stability Methods

It has been known that the vacancy defect in metal oxides could have different charged states. In α-Cr_2O_3, an O vacancy could have a charge state of 0 (V_{O}^{0}), +1 (V_{O}^{1+}), or +2 (V_{O}^{2+}) (it notes that the notations employed here are equivalent to Kröger-Vink notations V_O^x, $V_O^{\bullet}$, and $V_O^{\bullet\bullet}$ for O vacancies) and a Cr vacancy could have a charge state of 0 (V_{Cr}^{0}), -1 (V_{Cr}^{1-}), -2 (V_{Cr}^{2-}), or -3 (V_{Cr}^{3-}) (it notes that the notations employed here are equivalent to Kröger-Vink notations V_{Cr}^x, V_{Cr}', V_{Cr}'', and V_{Cr}''' for Cr vacancies). To account for the change in electrons, the "MAGMOM" line in the INCAR (input) file is altered to include the appropriate change in electrons.

It should also be mentioned that periodic boundary conditions employed in our DFT calculations would introduce spurious interactions between the charged periodic images. In this study, we applied the scheme proposed by Markov and Payne to eliminate the interaction between charged vacancies due to periodic boundary conditions [64]. In the hexagonal cell the dielectric constant differs parallel (11.7) and perpendicular (12.7) to the c-axis, where these values are the average of Table 4 in Ref. [65]. In our charged vacancy stability calculations we used the average of the two dielectric constants (12.2). We have examined the convergence of the calculated vacancy formation energy with respect to simulation cells by comparing the predictions for the neutral vacancies attained from the 2x2x1 (120 atoms) and 3x3x1 (270 atoms) cells. It is found that the predicted energies from the two different cells differed by merely 0.02 eV.

In this study, the formation energy (ΔE_f) of a charged vacancy in α-Cr_2O_3 crystal was calculated as [66]

$$\Delta \boldsymbol{E_f} = \boldsymbol{E_q^v} - \boldsymbol{E^{perf}} + \boldsymbol{\mu_i} + \boldsymbol{q\mu_e} \qquad \textbf{Equation 2-1}$$

In Equation 2-1, E^{perf} and $E_q{}^v$ is the calculated energy of the perfect Cr_2O_3 crystal and the defective Cr_2O_3 crystal containing a single vacancy with a charge of q, respectively; μ_i refers to the chemical potential of the O or Cr removed from the crystal to form a vacancy; and μ_e is the chemical potential of an electron in Cr_2O_3 crystal. For the determination of the chemical potentials of O and Cr in Cr_2O_3, we followed the computational method suggested by Finnis *et al.* [66]. Specifically, the

chemical potential of O was determined using the data from both the calculations and experiments, *i.e.*

$$\boldsymbol{\mu_O(p_{O_2}, T) = \frac{1}{3}\left[\mu^0_{Cr_2O_3} - 2\mu^0_{Cr(s)} - \Delta G_f^{Cr_2O_3}(p^0_{O_2}, T^0)\right] + \frac{1}{2}\Delta\mu_{O_2(g)}(T) + \frac{1}{2}k_B T ln\left(\frac{p_{O_2}}{p^0_{O_2}}\right)} \quad \textbf{Equation 2-2}$$

where, $\mu^0_{Cr_2O_3}$ and $\mu^0_{Cr(s)}$ are the chemical potentials of α-Cr_2O_3 and pure metal chromium at standard state and were approximated to be the energies of the respective crystal from the DFT calculations; $\Delta G_f^{Cr_2O_3}(p^0_{O_2}, T^0)$ is the standard Gibbs free energy change of the formation of chromia and was found from thermodynamic tables [67]; $\Delta\mu_{O_2(g)}(T)$ is the difference in the chemical potential of oxygen gas at temperature T and T^0 and was also attained from thermodynamic tables [67]. Moreover, the chemical potential of Cr was determined using the following relation.

$$\boldsymbol{\mu_{\mathrm{Cr}}(T) = \frac{1}{2}\left[\mu^0_{Cr_2O_3} + \Delta\mu_{Cr_2O_3}(T) - 3\mu_{\mathrm{O}}(p_{O_2}, T)\right]} \quad \textbf{Equation 2-3}$$

Here, the change in the chemical potential of α-Cr_2O_3 ($\Delta\mu_{Cr_2O_3}(T)$) due to temperature gain was again read from thermodynamic tables [57].

2.3 METHODS USED FOR ALUMINA

2.3.1 Calculation Specifics

A conventional hexagonal cell of the stoichiometric $Al_{12}O_{18}$ and 5x5x2 KPOINT integration was used to determine bulk properties by Lei [14] using the same methods as mentioned for chromia. All alumina grain boundary calculations use KPOINTS of 5x5x1 gamma integration, with an energy cutoff of 500eV and the Hellman-Feynman force acting on each ion to be less than $1x10^{-4}$ eV/Å. For DOS calculations KPOINTS were increased to 12x12x1.

The cell used for $\Sigma 11\{10\bar{1}1\}/\{10\overline{1\bar{1}}\}$ grain boundary calculations contains 180 atoms (108 O and 72 Al) and is based off the Kenway model (mentioned above in Section 1.4) [43, 44]. For the calculations with 1Å separation distance, the vacuum is approximately 11.4 Å to ensure no interaction between the grains as they repeat in the z-direction. The space between grains is fixed to 1Å for all contour plots, as suggested by Nakawaga [19]. For grains with Hf/Y, a Hf/Y replaces an Al atom as suggested by pervious results [20, 38, 40]. Replacing one Al atom corresponds to approximately 17at% surface coverage of the dopant within the grain boundary, and approximately 33at% when two Al atoms are replaced, this also corresponds to 0.56at% and 1.1at% for the complete simulation cell respectively.

2.3.2 Effects of Doping

To compare the effects of various Hf and Y concentrations, energy contour plots are created using ‘contourf’ in Matlab. Points for interpolation are created using the ‘course’ and ‘fine’ grids. Both grids contain points every 0.25 in the x- and y-directions, resulting in 16 points each, where points

are generated by shifting the coordinates by the corresponding fraction of the unit cell as can be seen in Figure 1. The difference comes from the original point, where the course grid begins at (0,0) and the fine grid begins at (0.125, 0.125), resulting in 32 grid points. Additional points can be added to help better define some of the minima valleys. Points are also added at the local minima in each valley, which is located using an in-house algorithm. For the energy contour plots atoms in the top and bottom layers are fixed (Figure 1b), to simulate the grain boundary in bulk, and other atoms are only allowed to relax in the z-direction.

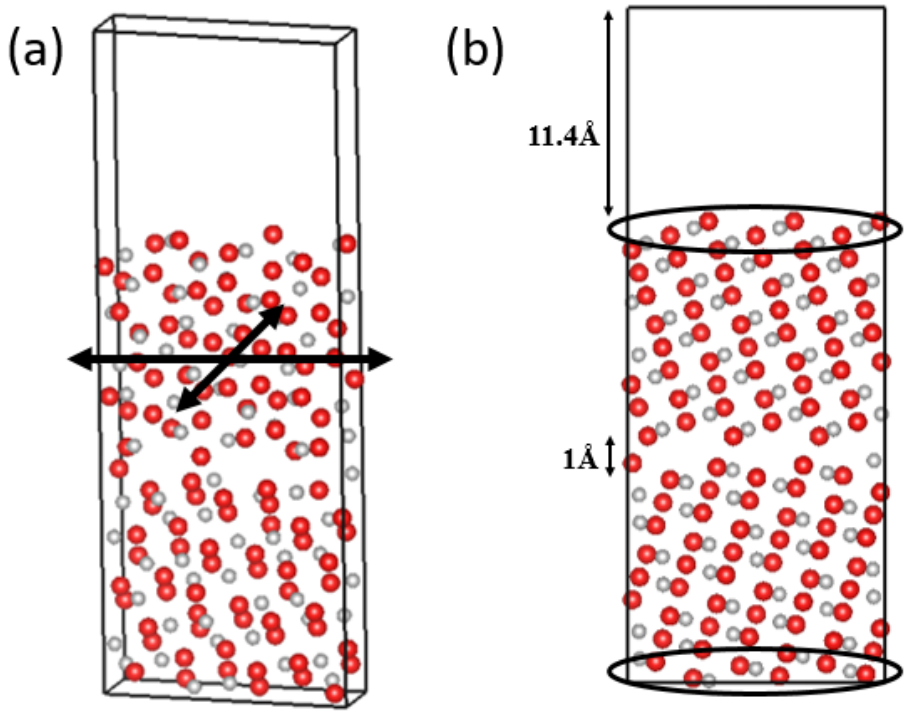

Figure 1. a) Schematic showing how the top grain boundary is shifted with respect to the bottom grain boundary. b) Circled atoms are fixed in position

2.3.3 Grain Boundary Energy

Grain boundary energy is calculated to explore the energy per area for each local minima grain boundary. To calculate grain boundary energy Equation 2-4 is used, where E_{cell} is the energy of the grain boundary in the simulation cell, N is the number of atoms (180), E_{bulk} is the energy per atom in the bulk phase, and A is area. Taking into consideration an alloying element, additional energy terms are included as seen in Equation 2-5, where $E_{M=(Hf, Y)}$ and E_{Al} correspond to the energy in their bulk phase and x is the number of alloying elements.

$$E_{bulk} = \frac{E_{cell} - N * E_{bulk}}{A} \qquad \textbf{Equation 2-4}$$

$$E_{bulk} = \frac{E_{cell} + xE_{M} - E_{Al} - N * E_{bulk}}{A} \qquad \textbf{Equation 2-5}$$

3.0 CHROMIA DIFFUSION

We computationally studied the lattice diffusion through the ion-vacancy exchange mechanism in α-Cr_2O_3 crystal using the first-principles DFT and DFT+U calculation methods*. For both O and Cr vacancies, we have identified four elementary diffusion paths in α-Cr_2O_3 crystal. Our DFT+U calculations predict that the O vacancy with charge +2 (V_O^{2+}) is stable when Fermi energy is near to valence band maximum; whereas, the Cr vacancy with charge -3 (V_{Cr}^{3-}) is stable when Fermi energy is close to conduction band minimum. Moreover, the DFT+U calculations predict that the migration energy for V_O^{2+} diffusion varies from 1.18 to 2.98 eV; whereas, that for V_{Cr}^{3-} diffusion varies from 2.02 to 2.59 eV, close to experimental data. Importantly, it is found that the DFT+U method describes α-Cr_2O_3 crystal better in terms of the magnetism, band gap, charge state of vacancies, and migration energies for charged vacancy diffusion as compared to the DFT method.

Upon finding the DFT+U method to provide more accurate results, Cr and O interstitials are examined. Cr interstitials were examined in an empty octahedral site and a local stable position found in a diffusion path, finding Cr ions are only stable in the octahedral site. O interstitials were placed in an oxygen layer and in an empty octahedral site, where O in the octahedral site was stable the ion in the oxygen layer resulted in a large rearrangement of the local structure.

3.1 BULK RESULTS

Bulk α-Cr_2O_3 crystal has a space group of $R\bar{3}c$ and a rhombohedral primitive unit cell with 10 (4 Cr and 6 O) atoms as shown in Figure 1a. Conventionally, crystalline chromia is represented with a hexagonal unit cell (shown in Figure 1b) consisting of 30 atoms (12 Al and 18 O atoms). In the crystal lattice, O atom occupies a tetrahedral site enclosed by four nearest neighboring Cr atoms (denoted as four-fold coordinated); whereas, Cr atom occupies an octahedral site enclosed by six nearest neighboring O atoms (denoted as six-fold coordinated). It is important to note that the Cr atoms occupy only 2/3 of the possible octahedral sites formed by the O atoms in the lattice of Cr_2O_3 crystal.

It should be noted that Cr_2O_3 crystal is an antiferromagnetic material, in which the net spin (i.e., magnetic moment) of a Cr ion is opposite to those of its neighboring Cr ions, below 307K [69, 70]. Consequently, the most stable spin configuration of Cr_2O_3 was adopted as the one that, if viewed in Figure 1a, the spins of the chromium ions were arranged as a $+ - + -$ spin sequence along the [111] axis of the rhombohedral cell [62]. Or, if viewed in Figure 1b, the spins of the Cr ions were aligned antiparallel to each other in both the metallic bilayers in the basal (0001) plane and along the [0001] direction normal to the basal plane of the conventional hexagonal unit cell [71].

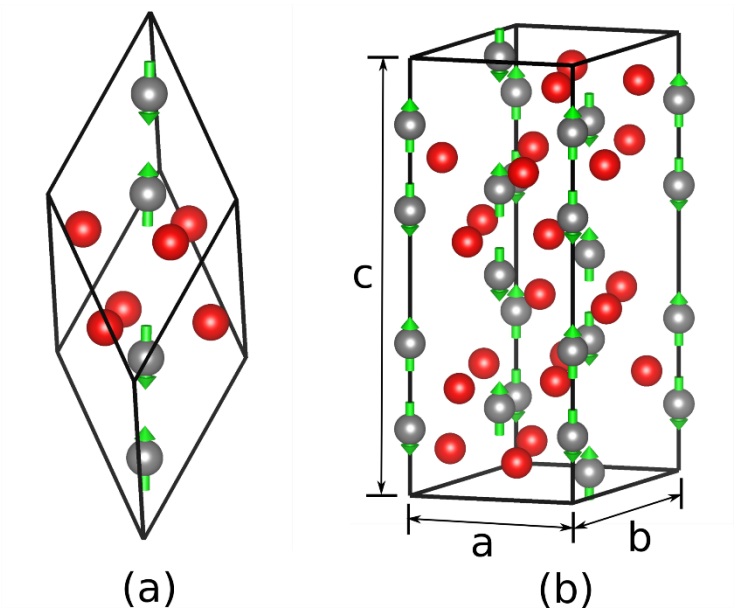

Figure 2. (a) Primitive rhombohedral unit cell and (b) conventional hexagonal unit cell of α-Cr2O3 crystal, where a, b and c are the [$\mathbf{2\bar{1}\bar{1}0}$], [$\mathbf{\bar{1}2\bar{1}0}$], and [0001] direction respectively. In the figure, the red spheres represent oxygen (O) atoms and the gray spheres represent chromium (Cr) atoms. The arrows indicate the magnetic moment directions of the Cr atoms in an antiferromagnetic α-Cr2O3.

In Table 1, we present some predicted physical properties of bulk α-Cr_2O_3 crystal from our DFT and DFT+U calculations and experimental results. It is noticeable that both our DFT and DFT+U calculations gave reasonably good results on the structural parameters (*a*, *c*, Cr-Cr(A) and Cr-Cr(B)) of Cr_2O_3 crystal, within less than 3.3% deviation from experimental values [72]. In contrast, the predictions on magnetic property and band gap from the two computational methods differ appreciably from the experimental values and from each other. As compared to the experimental value, [73] our DFT and DFT+U predictions overestimated the magnitude of the magnetic moment on each Cr atom by 8.1% and 16.1%, respectively. More noticeably, our DFT method predicted a small band gap (1.40 eV) which is 58.8% lower than the experimental

value of 3.4 eV [74], whereas our DFT+U method predicted the band gap of Cr_2O_3 crystal to be 3.26 eV which is only 4.1% lower than the experimental result.

Table 1. Lattice parameters *a* and *c*, Cr-Cr layer separations (short Cr-Cr (A) and long Cr-Cr (B) distances) along the c-axis, magnetic moment μ on Cr, and band gap E_g of bulk α-Cr_2O_3 crystal predicted from our *DFT* and DFT+U calculations. For comparison, we also list previous theoretical predictions [17] and experimental data [72, 73, 74].

	DFT (this work)	DFT+U (this work)	DFT+U [17]	Expt.
a (Å)	4.945	5.054	5.074	4.951 [72]
c (Å)	13.813	13.862	13.850	13.566 [72]
Cr-Cr (A) (Å)	2.638	2.716	2.717	2.650 [72]
Cr-Cr (B) (Å)	4.269	4.125	4.027	4.133 [72]
μ (μ_B/Cr atom)	2.68	2.88	3.10	2.48 [73]
Eg (eV)	1.40	3.26	2.80	3.4 [74]

In the previous DFT+U calculations, the GGA Perdew-Wang (PW91) exchange-correlation functional and an effective on-site Coulomb interaction parameter U= 5.0 eV were employed [17]. As described in Section 2.2.1, we used the GGA PBE functional and a U value of 4.5 eV in our DFT+U calculation. Comparing the predictions in Table 1 from the two DFT+U calculations, we find that our DFT+U calculation results on Cr magnetic moment and band gap agree better with experimental data.

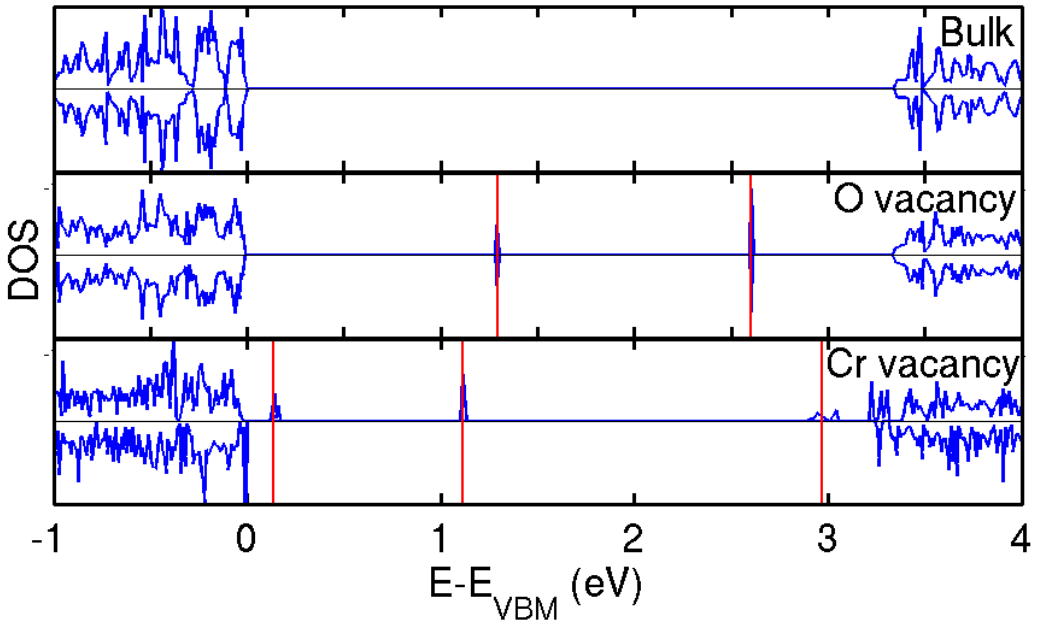

Figure 3. Predicted total density of states of α-Cr_2O_3 bulk crystal (modeled using a 120 ions supercell) and the same supercell containing a single O or Cr vacancy from our DFT+U calculations. The red lines mark the locations of defect states introduced by the vacancies.

In Figure 2, we plot the calculated density of states (DOS) for a perfect and defective (with vacancy) Cr_2O_3 crystal using the DFT+U method. Our results show that an O vacancy introduces two extra defect states at 1.29 eV and 2.61 eV above the valence-band maximum (E_{VBM}) inside the bad gap, whereas a Cr vacancy introduces three defect states at 0.14 eV, 1.11 eV, and 2.97 eV above E_{VBM}. Consequently, the vacancies with different charges will lead to different occupancy at these defects states. For example, the defect state at 1.29 eV will be fully occupied for vacancy V_O^0, however for V_O^{2+} the defect states are empty. Similarly, for Cr vacancies, the defect states are empty for V_{Cr}^0 and the defect states at 0.14 and 1.11 eV will be fully occupied for vacancy V_{Cr}^{3-}.

Associated with the introduction of these electronic defect states, the charged vacancies may also change the distribution of magnetic moments on the surrounding ions. In bulk α-Cr_2O_3 crystal, our DFT+U calculations predict that O ions have no magnetic moments whereas Cr ions have magnetic moments about 2.88 μB (see Table 1) in an antiferromagnetic arrangement. Our DFT+U calculations further indicate that the O vacancies cause little changes on the magnetic moments of the ions in the crystal. In contrast, the Cr vacancies could induce appreciable changes in the distribution of the magnetic moments in their surrounding ions, depending on their charge states. In this regard V_{Cr}^{0} is predicted to induce a magnetic moment of 0.29 μB on each of the six adjacent O ions whereas V_{Cr}^{3-} is found to induce a negligible magnetic moment of 0.01 μB on its surrounding O ion.

In a perfect α-Cr_2O_3 crystal, each O ion occupies a tetrahedral site enclosed by four nearest neighboring Cr ions (i.e., Cr tetrahedron) whereas each Cr ion occupies an octahedral site enclosed by six nearest neighboring O ions (i.e., O octahedron). Consequently, we define in this study the volume of the surrounding Cr tetrahedron to be the volume of an O ion and the volume of the surrounding O octahedron to be the volume of a Cr ion in α-Cr_2O_3, respectively. In this study, we predicted that the volume of O ions was about 3.10 $Å^3$ (DFT) and 3.34 $Å^3$ (DFT+U); whereas, the volume of Cr ions was about 10.48 $Å^3$ (DFT) and 10.87 $Å^3$ (DFT+U) in a perfect crustal of α-Cr_2O_3. Furthermore, we calculated the volumes of the Cr tetrahedron enclosing a relaxed O vacancy with different charges and the volumes of O octahedron enclosing a relaxed Cr vacancy with different charges. Both our DFT and DFT+U results indicate that the O vacancy with a zero charge (V_{O}^{0}) has a slightly smaller volume than the O ion whereas the Cr vacancy with a zero charge (V_{Cr}^{0}) has a volume about 17% larger than the Cr ion. Moreover, with an increase in valence charge, the volume of the O vacancy increases considerably. As can be seen from our DFT+U results, the

volume of the V_O^{1+} and V_O^{2+} is about 13.3% and 30.3% larger than that of V_O^0, respectively. In contrast, the volume of the Cr vacancy was found to vary not much (less than 1.2%) with its valence charge.

A qualitative model based on molecular-orbital theory has been proposed to explain the relation of the electronic and structural properties of oxygen vacancy in rutile TiO_2 [75]. Consistent with that model, we found that the outward relaxation of the Cr ions surrounding an O vacancy could lead to a significant (about 1.22 eV) upshift in the defect level of the O vacancy. Thus, the lattice relaxation around an O vacancy is strongly unfavored (i.e., small volume contraction as observed) for V_O^0 which has two electrons occupying the defect level, whereas it is favored (i.e., large volume expansion as observed) for V_O^{2+} which has no electron at its defect level. In contrast, we found that the outward relaxation of the O ions surrounding a Cr vacancy just caused a relatively small (about 0.03 eV) downshift in the defect level of the Cr vacancy. Consequently, the extent of lattice relaxation around a Cr vacancy exhibits little dependence on the number of electrons occupying the defect level of the Cr vacancy.

3.2 CHARGED VACANCY

In this study, the vacancy defect in α-Cr_2O_3 crystal was generated by removing one O or Cr ion from a 2x2x1 conventional hexagonal supercell crystal. For a perfect chromia crystal, a 2x2x1 conventional hexagonal supercell contains 48 Cr ions and 72 O ions. Thus, we modeled the structure of vacancy defects at a concentration of 0.83at% here. Consequently, the equilibrium structure of a charged vacancy was determined in this study by optimizing the structure of the

2x2x1 hexagonal supercell containing the vacancy and the correct number of electrons required by the charge state of this vacancy using both the DFT and DFT+U methods.

Figure 3 we present our DFT+U prediction for the variation of the charge states of the vacancies as a function of the chemical potential energy of electrons (μ_e) (as described in Section 2.2.3). At a given μ_e, the stable charge state of a vacancy is defined as the one having the lowest defect formation energy among all the possible charge states. Taking reference value of E_{VBM} in α-Cr_2O_3 as zero, we found from our DFT+U results in Fig. 3 that that V_O^0 would be the most stable O vacancy when μ_e is greater than 1.54 eV whereas V_O^{2+} would be the most stable O vacancy when μ_e is below 0.72 eV. Regarding various charged Cr vacancies, our DFT+U results predicted that the stable region of μ_e for V_{Cr}^0, V_{Cr}^{1-}, V_{Cr}^{2-}, and V_{Cr}^{3-} was from 0.0 eV (i.e., E_{VBM}) to 0.66 eV, from 0.66 eV to 1.18 eV, from 1.18 eV to 1.62 eV, and greater than 1.62 eV, respectively. Consequently, our DFT+U calculations suggest that V_O^{2+} and V_{Cr}^0 vacancies would co-exist in the α-Cr_2O_3 samples whose Fermi energy is near to their valence band maximum whereas V_O^0 and V_{Cr}^{3-} vacancies would co-exist in the α-Cr_2O_3 samples whose Fermi energy is close to their conduction band minimum. In contrast to the DFT+U predictions, our DFT calculations predicted that V_O^0 would be the most stable O vacancy for all the values of μ_e.

For the DFT results (not shown), only the neutral vacancy was stable for O. This result is illogical, due to binding nature of oxidation and reduction reactions, where oxygen takes electrons from the chromium atoms resulting in an anion. Cr charge stability follows a similar curve as the DFT+U results, however, the stabilities of $V_{Cr}^{1-} and\ V_{Cr}^{2-}$ are more pronounced, resulting in a smaller range in which V_{Cr}^{3-} is stable. In DFT+U for $V_{Cr}^{3-}\ and\ V_O^0$ to be stable ε_f must be greater than 1.62 eV (approximately half way though the band gap), while for DFT it must be greater than 1.11 eV (about 60% through the band gap).

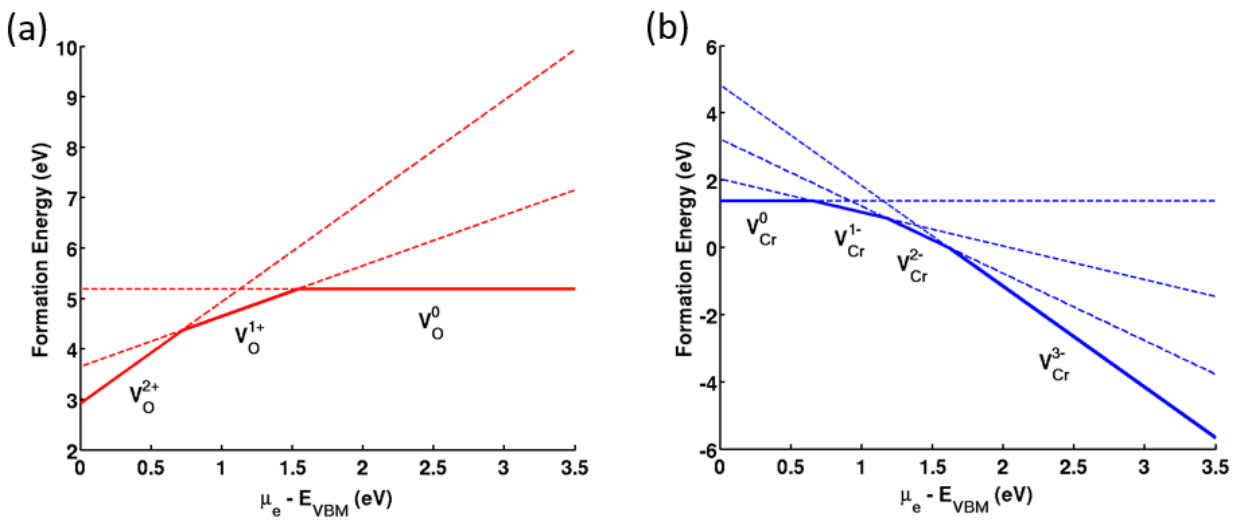

Figure 4. Variation of the formation energy of charged (a) oxygen and (b) chromium vacancies, calculated using the DFT+U method, as a function of the chemical potential of electrons in α-Cr_2O_3 crystal. The vacancy formation energies were calculated at condition of T=1300 K and P_{O2}=0.2 atm. In the figure, the dashed lines show the linear changes of the formation energy of a vacancy with a given charge, whereas the solid lines depict the changes in the most stable charge state of vacancies with varying μ_e.

3.3 VACANCY DIFFUSION

3.3.1 Elementary Diffusion Paths

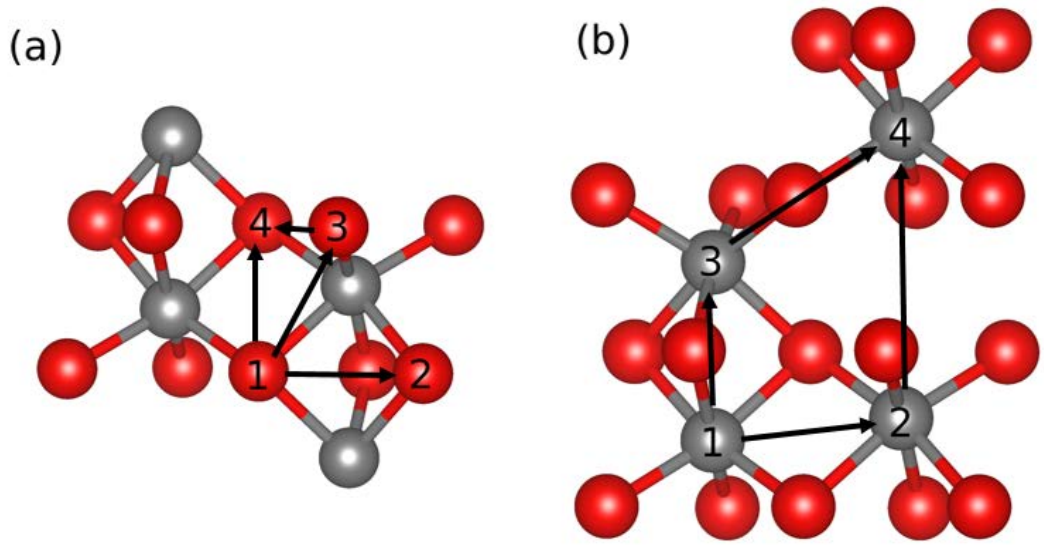

Figure 5. Schematic of four elementary a) oxygen and b) chromium diffusion jumps in bulk Cr_2O_3. In the figure the red atoms are O and the gray are Cr.

Within the corundum crystal structure of α-Cr_2O_3, we have identified four elementary paths for O vacancy diffusion and four elementary paths for Cr vacancy diffusion. All the other long-range diffusion for O and Cr vacancies in Cr_2O_3 can be attained by combining these elementary jumps. We present the atomic structures of these elementary diffusion paths in Figure 4 and the calculated diffusion distances of these elementary diffusion paths in Table 2.

.

Referencing the conventional hexagonal unit cell (Figure 1b), there are alternating O and Cr layers along the [0001] direction. It notes that all the O ions at each (0001) O layer lie on a

same plane but have two types of separations (short O_1—O_2 and long O_3—O_4 shown in Figure 4a) with their adjacent O ions at the same plane. In contrast, the nearest neighboring Cr ions at each (0001) Cr layer are relaxed toward the opposite [0001] directions and thus form a buckling surface layer with about 0.03 Å difference in the [0001] coordinates of the Cr ions. However, there is only one type of separation (Cr_1—Cr_2 in Figure 4b) between the nearest neighboring Cr ions within a (0001) Cr layer. In addition to the in-(0001)-plane diffusion of O and Cr vacancies, the O vacancy can further diffuse across neighboring (0001) planes along either an exact [0001] jump (O_1—O_4 in Figure 4a) or a tilted jump (O_1—O_3 in Figure 4a) whereas the Cr vacancy across neighboring (0001) planes along either an exact [0001] jump (Cr_1—C_3 in Figure 4b) or a tilted jump (Cr_3—Cr_4 in Figure 4b). Moreover, the Cr vacancy is found to be able to directly diffuse across two (0001) planes along a [0001] jump (Cr_2—Cr_4 in Figure 4b).

Table 2. Diffusion distances (in unit of Å) and descriptions of elementary diffusion paths for O and Cr vacancies in α-Cr_2O_3 crystal.

Diffusion Paths	Diffusion distance		Description
	DFT	DFT+U	
O vacancy			
$O_1 \rightarrow O_2$	2.66	2.66	within a (0001) plane of O
$O_1 \rightarrow O_3$	2.87	2.91	bridging two (0001) planes of O
$O_1 \rightarrow O_4$	2.78	2.79	bridging two (0001) planes of O
$O_3 \rightarrow O_4$	2.96	3.06	within a (0001) plane of O
Cr vacancy			
$Cr_1 \rightarrow Cr_2$	2.87	2.95	within a (0001) plane of Cr
$Cr_1 \rightarrow Cr_3$	2.63	2.72	bridging two (0001) Cr planes separated by one O layer
$Cr_2 \rightarrow Cr_4$	4.27	4.22	bridging two (0001) Cr planes separated by two O layers
$Cr_3 \rightarrow Cr_4$	3.47	3.48	bridging two (0001) Cr planes separated by one O layer

3.3.2 Diffusion of V_{O}^{2+} and V_{Cr}^{3-}

Using the CI-NEB computational method [63], we have determined the minimum-energy pathways, the transition states, and hence the migration energies for the charged O vacancy (V_O^{2+}) (i.e., O^{2-} ion) and Cr vacancy (V_{Cr}^{3-}) (i.e., Cr^{3+} ion) diffusion in α-Cr_2O_3 crystal. In Figure 5 and Figure 6, we plot the minimum-energy pathways and transition states for V_O^{2+} and V_{Cr}^{3-} diffusion paths, respectively. Moreover, we report the calculated the migration energies for V_O^{2+} and V_{Cr}^{3-} diffusion along various elementary diffusive paths in Table 3.

Our DFT+U results in Figure 5 reveal that all the V_O^{2+} diffusions in α-Cr_2O_3 crystal follow simple minimum-energy paths that contain only one transition state. Furthermore, our calculations predict that the migrating O ion at the transition state becomes fourfold coordinated in diffusion path $O_1 \rightarrow O_2$ whereas two-fold coordinated in diffusion paths $O_1 \rightarrow O_3$, $O_1 \rightarrow O_4$, and $O_3 \rightarrow O_4$, as compared to the four-fold coordinated O ions in the bulk crystal. It appears that low coordination number of the migrating O ion in the transition state is correlated to high migration energy for V_O^{2+} lattice diffusion.

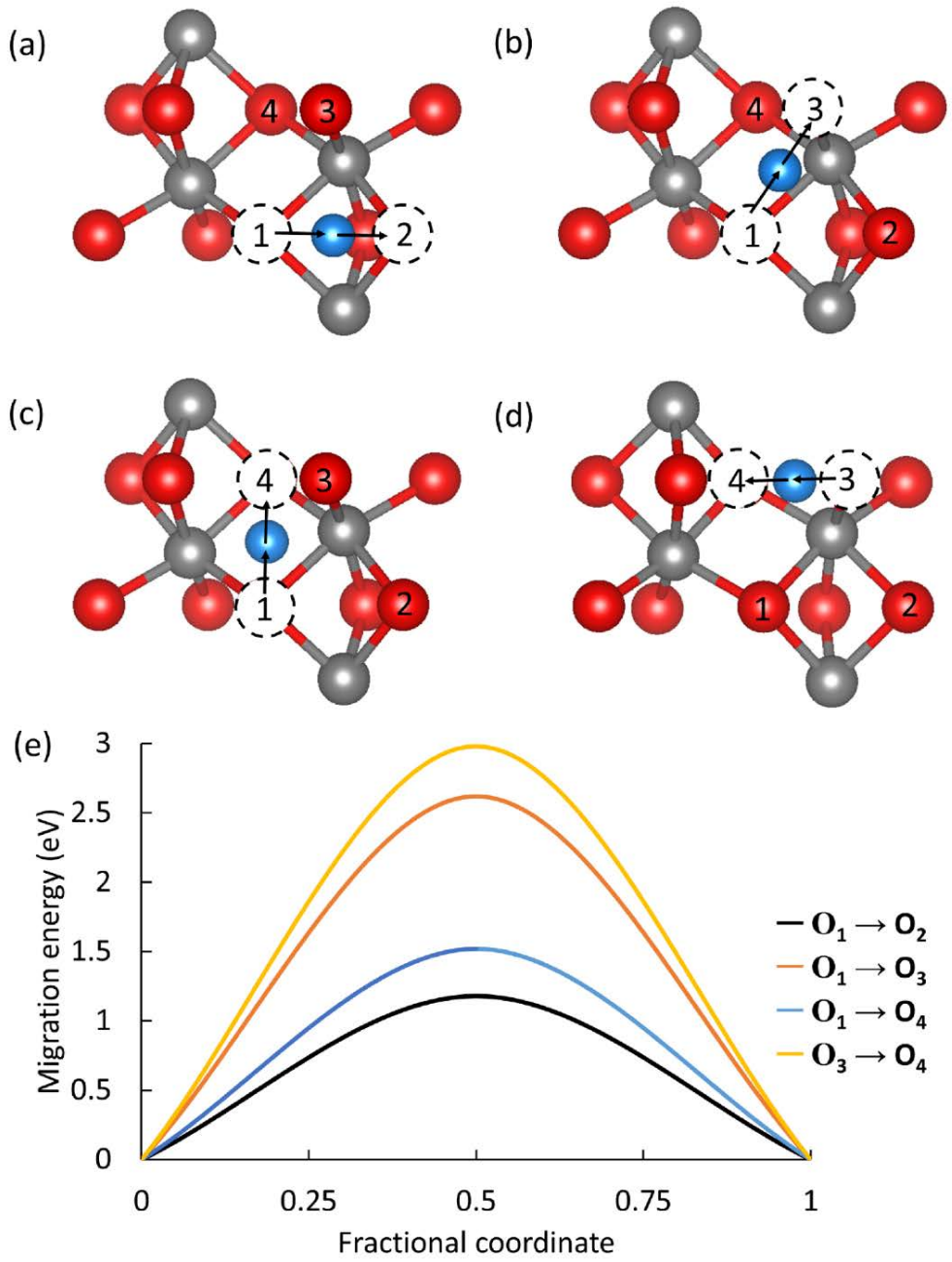

Figure 6. Atomistic structures of the predicted minimum energy pathway for O vacancy ($\boldsymbol{V_O^{2+}}$) diffusion (a) $O_1 \rightarrow O_2$, (b) $O_1 \rightarrow O_3$, (c) $O_1 \rightarrow O_4$, and (d) $O_3 \rightarrow O_4$, and (e) variation of potential energy during O vacancy diffusion along these pathways, obtained from the DFT+U calculations. In (a-d), the red and gray spheres represent O and Cr ions, the dashed circles show the initial and final positions of O vacancy, the arrows point to the direction of diffusions, and the blue spheres mark the transition state positions of diffusive O^{2-} ion.

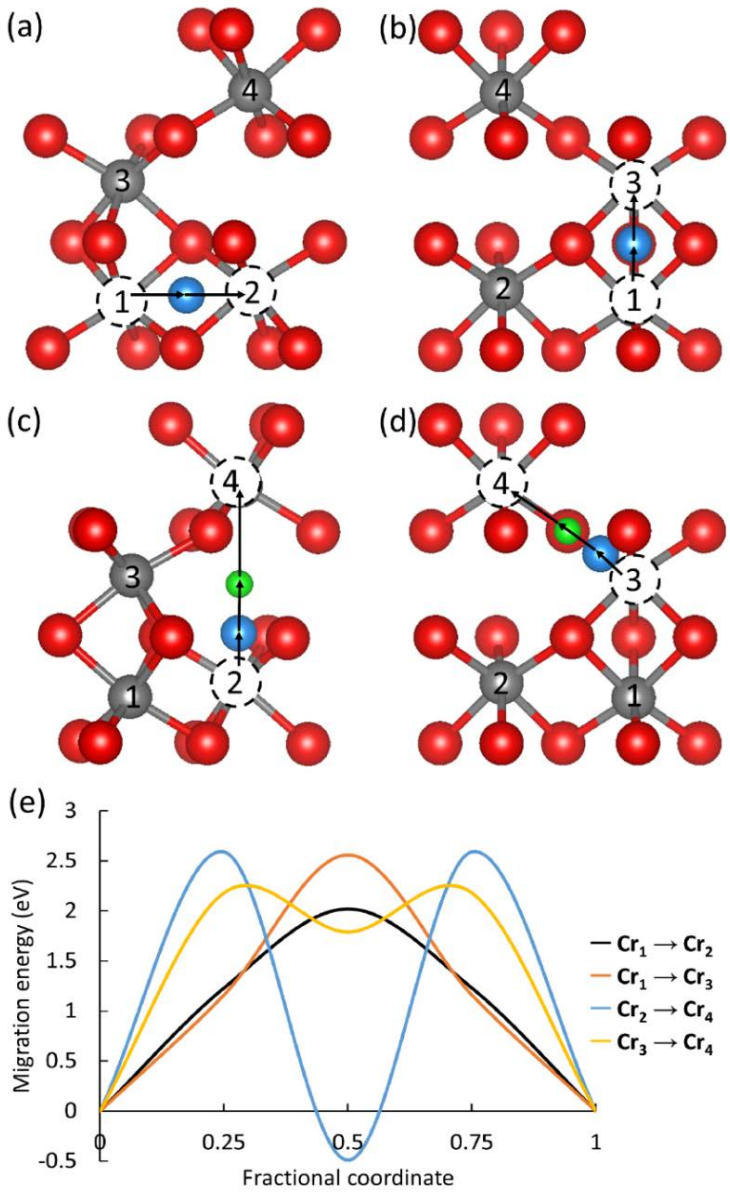

Figure 7: Atomistic structures of the predicted minimum energy pathway for Cr vacancy ($\boldsymbol{V_{Cr}^{3-}}$) diffusion (a) $Cr_1 \rightarrow Cr_2$, (b) $Cr_1 \rightarrow Cr_3$, (c) $Cr_2 \rightarrow Cr_4$, and (d) $Cr_3 \rightarrow Cr_4$, and (e) variation of potential energy during Cr vacancy diffusion along these pathways, obtained from the DFT+U calculations. In (a-d), the red and gray spheres represent O and Cr ions, the dashed circles show the initial and final positions of Cr vacancy, the arrows point to the direction of diffusions, and the blue spheres mark the transition state positions of diffusive Cr^{3+} ion. In (c-d), the green balls mark the locally minimum-energy positions of diffusive Cr ion along the diffusion pathways.

Our DFT+U results in Figure 6 show that the V_{Cr}^{3-} diffusions follow simple minimum-energy paths for diffusion $Cr_1 \rightarrow Cr_2$ and $Cr_1 \rightarrow Cr_3$ paths, but complex minimum energy paths (containing one locally minimum-energy configuration and two transition states) for $Cr_2 \rightarrow Cr_4$ and $Cr_3 \rightarrow Cr_4$ diffusion. The same as Lei's previous results in α-Al_2O_3 [14], the locally minimum-energy configuration in diffusion $Cr_2 \rightarrow Cr_4$ and $Cr_3 \rightarrow Cr_4$ is that the migrating Cr ion lies right in between two facing triangular facets of adjacent O octahedrons and thus is a Cr Frenkel defect in α-Cr_2O_3 crystal. Shown in Figure 6e, our DFT+U calculations predict that the Cr Frenkel defect along diffusion $Cr_2 \rightarrow Cr_4$ has an energy 0.50 eV lower than a relaxed Cr vacancy whereas the Cr Frenkel defect along diffusion $Cr_3 \rightarrow Cr_4$ has an energy 1.79 eV higher than a relaxed Cr vacancy. In this work, we studied only the diffusion of the Cr Frenkel defect to a vacant lattice site following ion-vacancy exchange diffusion mechanism, as shown in Figure 6. It is worth mentioning that the Cr Frenkel defect can also possibly diffuse to an adjacent interstitial site following interstitial diffusion mechanism.

Furthermore, our calculations predict that the migrating Cr ion at the transition state becomes four-fold coordinated in diffusion paths $Cr_1 \rightarrow Cr_2$ and $Cr_3 \rightarrow Cr_4$ and three-fold coordinated in diffusion paths $Cr_1 \rightarrow Cr_3$ and $Cr_2 \rightarrow Cr_4$, as compared to the six-fold coordinated Cr ions in the bulk crystal. It is noticeable that the transition state of diffusion $Cr_1 \rightarrow Cr_2$ has a higher oxygen coordination number (four) than that (three) at the transition state of diffusion $Cr_1 \rightarrow Cr_3$. Moreover, the predicted migration energy for $Cr_1 \rightarrow Cr_2$ is found to be lower than that for $Cr_1 \rightarrow Cr_3$, even though diffusion $Cr_1 \rightarrow Cr_2$ has a longer diffusion distance than $Cr_1 \rightarrow Cr_3$. Hence, our results suggest that the migration energy for Cr ions strongly depends on the oxygen coordination number of the transition state for the diffusion in α-Cr_2O_3 crystal. The general trend is that high oxygen coordination number corresponds to low migration energy. Our results here

are consistent with previous prediction that Li ions prefer to maintain high oxygen coordination during diffusion in Li_2CO_3 for facile transportation [76].

Table 3. Predicted migration energies (in unit of eV) of charged $\boldsymbol{V_O^{2+}}$ and $\boldsymbol{V_{Cr}^{3-}}$ vacancies along the elementary lattice diffusion paths (shown in Fig. 4) in α-Cr_2O_3 crystal.

Diffusion path	DFT (this work, GGA-PBE)	DFT (Ref. 16, GGA-PW91)	DFT+U (this work, GGA-PBE)	DFT+U (Ref. 17, GGA-PW91)
O vacancy				
$O_1 \rightarrow O_2$	1.32	1.15	1.18	2.21
$O_1 \rightarrow O_3$	2.36	--	2.62	2.35
$O_1 \rightarrow O_4$	1.69	--	1.52	--
$O_3 \rightarrow O_4$	2.20	--	2.98	3.22
Cr vacancy				
$Cr_1 \rightarrow Cr_2$	1.91	2.02	2.02	2.73
$Cr_1 \rightarrow Cr_3$	2.09	--	2.56	3.21
$Cr_2 \rightarrow Cr_4$	2.14	--	2.59	2.57
$Cr_3 \rightarrow Cr_4$	2.08	--	2.18	--

3.3.3 Diffusion of V_{O}^{0} and V_{Cr}^{0}

In Figure 3, our DFT+U results predicted that V_{O}^{2+} and V_{Cr}^{0} vacancies would co-exist in the α-Cr_2O_3 samples whose Fermi energy is near to their valence band maximum whereas V_{O}^{0} and V_{Cr}^{3-} vacancies would co-exist in the α-Cr_2O_3 samples whose Fermi energy is close to their conduction band minimum. To acquire a full picture of vacancy diffusion in α-Cr_2O_3 crystals, we have also determined the migration energies for the neutral O vacancy (V_O^0) and Cr vacancy (V_{Cr}^0) diffusion in α-Cr_2O_3 crystal using the CI-NEB computational method [63]. In Table 4, we give the calculated migration energies for charge-neutral V_O^0 and V_{Cr}^0 diffusing along various elementary diffusive paths.

Both our DFT and DFT+U results in Table 4 indicate that the migration energy for V_{O}^{0} diffusion via any diffusive paths is higher than that of V_{O}^{2+} diffusion (the difference could be as high as 1.19 eV manifested in our DFT+U results for $O_1 \rightarrow O_3$) whereas the migration energies for V_{Cr}^{3-}diffusion are lower than those of V_{Cr}^{0} diffusion (the difference could be as large as 0.99 eV manifested in our DFT+U results for $Cr_1 \rightarrow Cr_3$). Consequently, we predicted that the vacancy diffusion strongly depends on the charge state of the vacancy involved in α-Cr_2O_3 crystal. This charge-dependent vacancy diffusion was also predicted in alumina crystal in a previous study [15] and was attributed to the energy shift in the electronic defect state of the charged vacancies during diffusion [15].

Table 4. Comparison of the predicted migration energies (in unit of eV) of charged ($\boldsymbol{V_O^{2+}}$ and $\boldsymbol{V_{Cr}^{3-}}$) and neutral ($\boldsymbol{V_O^0}$ and $\boldsymbol{V_{Cr}^0}$) vacancies along the elementary lattice diffusion paths (shown in Fig. 4) in α-Cr_2O_3 crystal.

Diffusion path	DFT		DFT+U	
O vacancy	V_O^{2+}	V_O^0	V_O^{2+}	V_O^0
$O_1 \rightarrow O_2$	1.32	2.27	1.18	2.35
$O_1 \rightarrow O_3$	2.36	3.56	2.62	3.81
$O_1 \rightarrow O_4$	1.69	2.32	1.52	2.67
$O_3 \rightarrow O_4$	2.20	3.06	2.98	3.71
Cr vacancy	V_{Cr}^{3-}	V_{Cr}^0	V_{Cr}^{3-}	V_{Cr}^0
$Cr_1 \rightarrow Cr_2$	1.91	2.10	2.02	2.58
$Cr_1 \rightarrow Cr_3$	2.09	2.56	2.56	3.55
$Cr_2 \rightarrow Cr_4$	2.14	2.45	2.59	3.10
$Cr_3 \rightarrow Cr_4$	2.08	2.22	2.18	2.71

Similarly, we find in this work that the O vacancy diffusion involves an upshift in the energy level of the defect state toward the conduction band of the α-Cr_2O_3 crystal. In Section 3.1, we have pointed out that there are two electrons occupying the defect states of vacancy V_O^0 but no electron on the defect states of V_O^{2+}. Consequently, the upshift in the defect states of O vacancy causes the migration energy of V_O^0 higher than that of V_O^{2+}. In contrast, we find that the Cr vacancy involves a downshift in the energy level of the defect state toward the valence band of the α-Cr_2O_3 crystal. Since the defect states are empty for V_{Cr}^0 but fully occupied by three electrons for vacancy V_{Cr}^{3-}, this downshift in the defect states of Cr vacancy causes the migration energy of V_{Cr}^{3-} lower than

that of V_{Cr}^{0}. Therefore, the shifts in the defect state during diffusion is also found be responsible for the charge-dependent migration energies given in Table IV for the vacancies in α-Cr_2O_3.

3.3.4 Discussion

Comparing our DFT and DFT+U calculation results in Table 3, we notice that the two computational methods give different predictions for the migration energies of V_O^{2+} and V_{Cr}^{3-} diffusion in α-Cr_2O_3 crystal. The discrepancy is found to be small for low-barrier diffusion but pronounced for high-barrier diffusion. For example, the predicted migration energies of low-barrier V_{Cr}^{3-} vacancy diffusion along $Cr_1 \rightarrow Cr_2$ differ by 0.11 eV whereas those of high-barrier V_O^{2+} diffusion along $O_3 \rightarrow O_4$ differ by 0.78 eV. As compared to the DFT method, the DFT+U method includes an additional correction term based on the Hubbard model and hence is believed to describe better the materials systems with localized electrons [61]. For Cr_2O_3 crystal with strongly localized electrons, our results in Table 1 indeed indicate that the magnetic moment of Cr and band gap predicted from the DFT+U method agree better with the experimental data than those from the DFT method.

Using isotope tracers and secondary-ion mass spectrometry, Saiboini *et al.* measured the diffusion profiles in experiments and further determined the migration energy for O self-diffusion to be 2.384 eV (range of P_{O_2}= 1x10^{-9}—1.6x10^{-16} and T=1100°C) [77] and for Cr self-diffusion to be 2.902 eV (range of P_{O_2}= 5x10^{-5}—3x10^{-13} and T=1200—1400°C) [78] in Cr_2O_3 single crystal. Consequently, we also found that the migration energies predicted from the DFT+U methods agree better with the experimental values than those from the DFT calculations.

In Table 3, we also gave the migration energies of charged V_{O}^{2+} and V_{Cr}^{3-} vacancies in α-Cr_2O_3 predicted from limited first-principles calculations. It is notable that, for both diffusion $O_1 \rightarrow O_2$ and $Cr_1 \rightarrow Cr_2$, our DFT+U results are very close to those from a prior DFT calculation [16], which was performed using the CASTEP code, ultrasoft pseudopotential, and GGA-PW91 approximation for exchange-correlation. Because only these two migration energies are reported in Ref. 16, we cannot exclude the possibility that the apparent agreement between our DFT+U and previous DFT methods might be accidental. Interestingly, our DFT+U results for diffusion $O_1 \rightarrow O_2$ and $Cr_1 \rightarrow Cr_2$ are dramatically lower by 1.03 eV and 0.71 eV respectively as compared to those from a prior DFT+U calculation [17], which differs from our calculations mainly in the value of effective on-site Coulomb interaction parameter U. Shown in Table 1, our DFT+U calculations gave better description for the Cr magnetic moment and band gap of α-Cr_2O_3 crystal than the DFT+U computation in Ref. 17. Hence, this study reveals that the effective on-site Coulomb interaction parameter U could have a strong effect on the predicted migration energy of defects in metal oxides and thus should be carefully chosen in the DFT+U calculations.

3.4 INTERSTITIAL ATOMS

Defects in Cr_2O_3 have been examined to help determine the diffusion mechanisms. It has been predicted that both interstitials and vacancies are both present in chromia. For example, Atkinson *et al.* simulated (using CASTEP) Schottky and anion Frenkel defects, which resulted in oxygen vacancies [79]. They also found that the concentration of Schottky and anion Frenkel defects will alter the number of Cr vacancies and O interstitials [79]. While examining the growth of chromia on chromium, Kofstad and Lillerud found the predominant point defects in chromia are chromium

interstitials at low oxygen activities, while a minority defect is oxygen vacancies at partial pressures near the decomposition of Cr_2O_3 [3].

To examine the stability of possible point defects in α-Cr_2O_3, a DFT+U examination of four interstitials (two for each Cr and O). As Cr does not fill all possible octahedral sites, both O and Cr are tested here and the stability is tested for charged and neutral cases. The meta-stable point shown in diffusion path $Cr_2 \rightarrow Cr_4$ (Figure 6d) will also be tested to determine if this position is stable. A second O interstitial to be tested is in the oxygen layer.

Currently, Schottky defects are not examined due to the size of the simulation cell. The current simulation cell contains 120 atoms (48 Cr ions and 72 O ions), a Schottky defect is stoichiometric, resulting in the removal of 2 Cr ions and 3 O ions, resulting in an unreasonable 4.2% vacancy concentration. In the same manner, Frenkel pairs will not be examined, as they pose a geometrical problem due to the limited size of the simulation cell.

3.4.1 Cr Interstitials

Cr interstitials were included in one of the empty octahedral sites and in a tetrahedral like site, both stable locations in the diffusion paths in Section 3.2. For both neutral Cr interstitials, it was found that the spin of the Cr does not matter, the defect energy remained the same. This is due to the antiferromagnetic ordering shown in Figure 1, where nearest neighbor Cr atoms contain the opposite spin. The interstitial atom then always has the same spin as the Cr above/below and the opposite of the other.

Figure 7 below shows the initial and final positions for both interstitials, where Figure 7a corresponds to the stable position for diffusion path $Cr_2 \rightarrow Cr_4$ and Figure 7b corresponds to the stable position for $Cr_3 \rightarrow Cr_4$ (Figure 6). For the octahedral site (Figure 7a), the initial and final

positions are in the same location, indicating the position is stable. However, for the tetrahedral site (Figure 7b), this is not the case, during the relaxation process the atom transitioned to a local, empty octahedral site indicating the position is not stable. The effect of charge on a Cr ion is investigated for the stable octahedral site, and found to alter the stability of the interstitial as can be seen in Table 5.

Table 5. Change in defect energy for a Cr atom in an empty octahedral site based on charge.

Cr charge	Defect energy (eV)
3+	21.72
2+	15.75
1+	9.32
0	2.89
-1-	-3.49
2-	-10.06
3-	-16.69

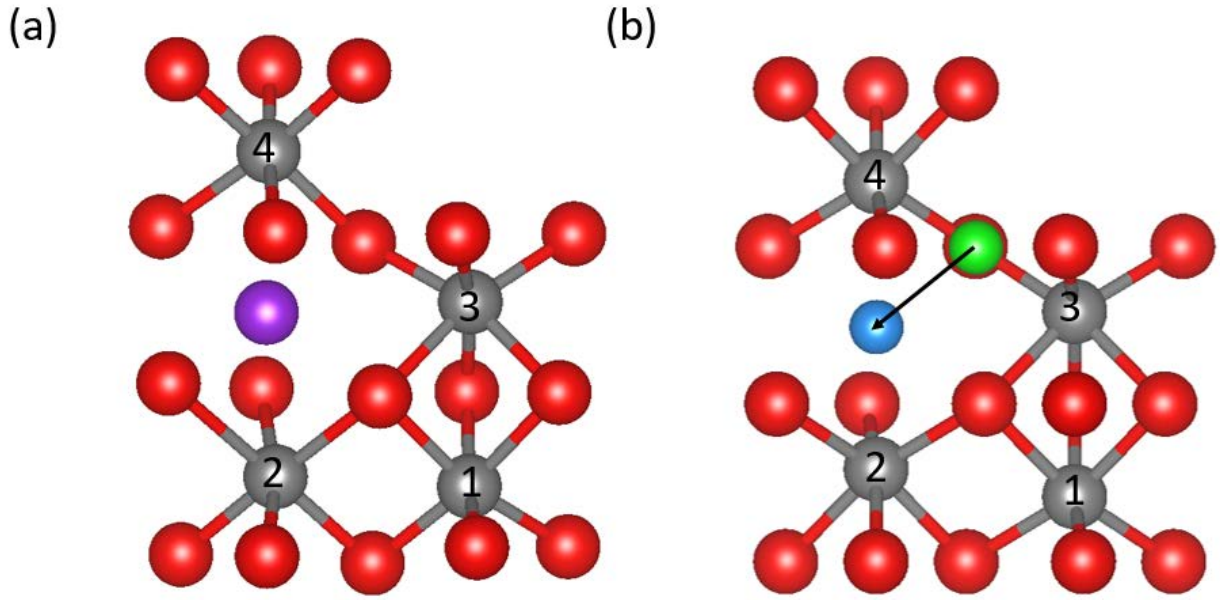

Figure 8 Interstitial positions for a) octahedral and b) tetrahedral Cr interstitials. Red balls are O, gray are Cr, green is the initial position of the interstitial, blue is the final position of the interstitial, and purple is final and initial positions in the same location.

3.4.2 O Interstitials

O was then tested in the same in the same octahedral site and placed within an oxygen layer. For the octahedral site, the O interstitial behaved the same as Cr and was stable.

Table 6 shows the energy change by adding an interstitial O atom.

Table 6 shows the defect energy as the charge of the O ion is changed. Counterintuitively, we observe simply adding an O interstitial to perfect chromia prefers to contain two less electrons.

Table 6. Change in defect energy for a O atom in an empty octahedral site based on charge.

O charge	Defect energy (eV)
2+	8.30
1+	4.92
0	0.27
1-	-4.23
2-	-9.04

However, as shown in Figure 8, the interstitial in the O layer was not stable. During relaxation, the non-stable O atom displaced a local Cr atom (circled in Figure 8b) into the O-layer below it. When examining the atomic structure of chromia, we can see the oxygen layers are close packed [80], and thus the additional oxygen atom results in a major atomic rearrangement and thus the lack of stability of this interstitial.

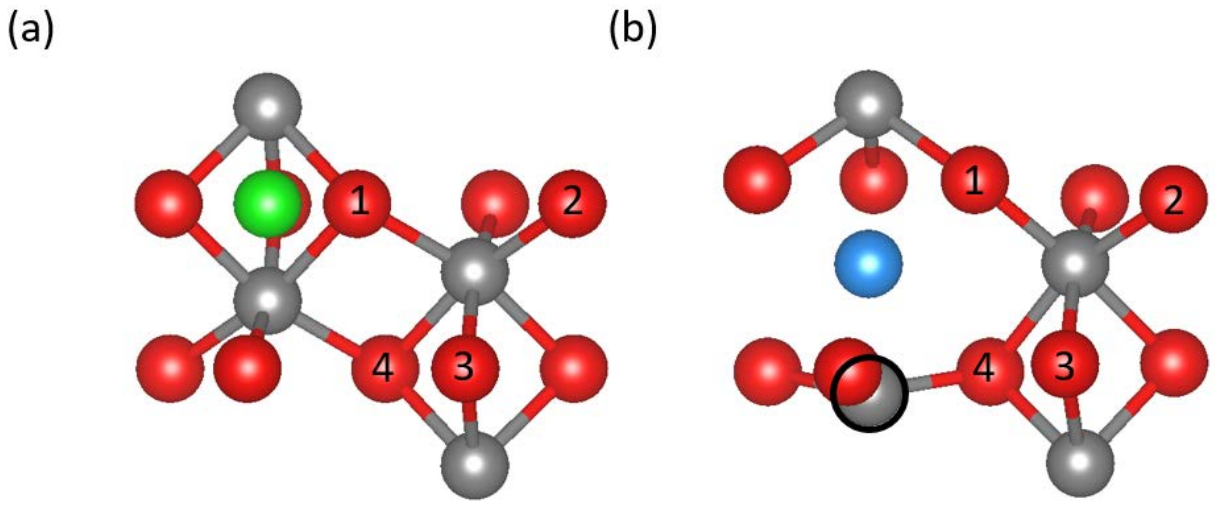

Figure 9 a) initial and b) final positions for O interstitial in an oxygen layer. Where red balls are O, gray balls are Cr, the green ball is the interstitial's starting position and the blue ball the final position.

3.5 CONCLUSIONS

In summary, we employed both DFT and DFT+U calculation methods to predict the migration energies for neutral (V_O^0 *and* V_{Cr}^0) and charged O (V_O^{2+}) and Cr (V_{Cr}^{3-}) vacancies in antiferromagnetic α-Cr_2O_3 crystal. More extensive than prior modeling studies, we investigated a complete set of four elementary diffusion paths for each of the vacancies. Benchmarked against experimental results, we found that the DFT+U method gave better predictions on the magnetism, band gap, charge state of vacancies, and migration energies for charged vacancy diffusion of α-Cr_2O_3 bulk crystal than the DFT method. Therefore, this study not only presents atomistic details and energetics about the lattice diffusion processes in α-Cr_2O_3 bulk crystal, but also suggests that the DFT+U method is preferred for computational study of defects and their diffusion in Cr_2O_3.

We have also shown for the interstitial sites tested, only the octahedral sites provide a stable location for both oxygen and chromium ions.

3.6 FUTURE WORK

The work discussed earlier focused on Cr_2O_3 bulk diffusion, however as stated by experimental groups, the bulk diffusion is not responsible for the observed diffusion constants [10, 11, 13]. This prompts an investigation into grain boundary diffusion behavior. Testing this for chromia, however, is computationally expensive, as one must use DFT+U calculations and take into consideration the antiferromagnetic behavior, with great computational cost. The same holds true for exploring more interstitial cases, the simulation cell must grow before more realistic interstitials and vacancies can be explored. As the systems examined above already push the upper bounds of current computational capabilities, one must wait for computers or code to improve.

In the case for grain boundary diffusion, one can look for a 'simpler' system, in which we turn to alumina which is non-magnetic and does not require the Hubbard (+U) correction. Both Cr_2O_3 and Al_2O_3 possess the same structure, space group of $R\bar{3}c$ and a rhombohedral primitive unit cell with 10 (4 Cr/Al and 6 O) atoms. Table 7 below shows the comparison of the work of a previous student Lei on alumina and this work on chromia. The lattice constants and separation distances are similar in value, while the differences can be attributed to the size of chromium atoms compared to aluminum. For the lowest activation energies, it is important to note that there may be differences in the energy the path that possess the lowest energy is the same. In this regard, we can examine an Al_2O_3 grain boundary as the preliminary step to studying a Cr_2O_3 grain boundary, as the same techniques can be used first with alumina to ensure they will work for chromia.

Table 7: Comparison between alumina and chromia lattice parameters and lowest diffusion activation energies for the neutral case, in all cases from atom1 to atom2. M is Cr for chromia and Al for alumina.

	Chromia DFT	Chromia DFT+U	Alumina DFT [14]
a (Å)	4.945	5.054	4.81
c (Å)	13.813	13.862	13.31
M-M (A) (Å)	2.638	2.716	2.682
M-M (B) (Å)	4.269	4.125	3.883
Eg (eV)	1.40	3.26	6.00
lowest O → O (eV)	2.27	2.35	3.58
lowest M → M (eV)	2.10	2.58	1.80

*This work was published previously [68]

4.0 GRAIN BOUNDARY OF ALUMINA

Alumina acts as a model starting point for understanding oxide diffusion, in this regard we examine the effects of reactive elements Y and Hf on properties of the $\Sigma 11\{10\bar{1}1\}/\{10\overline{\bar{1}1}\}$ grain boundary. Introducing a single Y atom to the grain boundary (0.6at% doping for the entire system, 17at% within the grain boundary) results shows small amount of changes in the DOS and geometric stabilities compared to the undoped case pointing to slower diffusion. Whereas 1Hf shows larger amounts of change indicating a greater amount of slowing for grain boundary diffusion. An increased concentration of 2Hf (33at% within the grain boundary and 1.2at% for the simulation cell) shows larger changes still when comparing grain boundary properties, thus slowing diffusion beyond that of 1Hf. In this regard we observe not only does the dopant effect diffusion, but the concentration does as well.

4.1 $\boldsymbol{\Sigma 11\{10\bar{1}1\}/\{10\overline{\bar{1}1}\}}$ GRAIN BOUNDARY

The $\Sigma 11\{10\bar{1}1\}/\{10\overline{\bar{1}1}\}$ grain boundary was chosen as a representative grain boundary of alumina as it has been observed experimentally and has begun being investigated theoretically [19, 20, 36]. Y was chosen as a dopant due to its behavior as a model case, same number of valence electrons

only having larger atomic size [35]. Hf, additional valence electron and increased atomic size, was also chosen as a dopant due to the improved oxidation behaviors previously observed [20, 21].

4.1.1 Alumina $\Sigma 11\{10\bar{1}1\}/\{10\overline{1\bar{1}}\}$ Grain Boundary

The structure for the (0,0) position for the alumina grain boundary can be seen in Figure 9a. Figure 9b shows the energy contour for a fixed 1Å separation distance where atoms are fixed in the x- and y- directions. It can be observed that there are three minima for the $\Sigma 11\{10\bar{1}1\}/\{10\overline{1\bar{1}}\}$ alumina grain boundary, marked with white crosses in Figure 9b. It is important to note that as one goes beyond one in shifting the atoms the pattern repeats. Thus the middle-top minima valley connects to the bottom-middle valley and the left-middle and right-middle valleys also connect. The three minima are found to have the same energy, varying by less than 0.05eV, indicating the probability of being in any of these configurations is nearly equivalent.

To understand how the minima contain the same energy, structural analysis was performed on the minima. Figure 10 shows the atomic layer of atoms in the top grain for the minima (1.108, 0.365). It can be seen in the figure that the Al atoms are spaced approximately every third in both the x-direction, $[2\bar{1}\bar{1}1]||[2\bar{1}\bar{1}\bar{1}]$, and y-direction, $[\bar{1}2\bar{1}0]$. If we compare the fractional coordinates of our three minima, we can see that they shift approximately one-third in the positive x-direction and negative y-direction, as indicated by the arrowed path in Figure 10. For example, start at (0.44, 0), if we translate (+0.33, -0.33) as approximated by Figure 10, the structure becomes (0.77, -0.33) however due to the repeating structure in the x- and y-directions the point becomes (0.77, 0.67) which is very similar to the minima found at (0.76, 0.7). Transitioning from (0.76, 0.7) results in (1.09, 0.37), which is similar to the point at (1.108, 0.365) This indicates that our three minima have nearly identical structures and thus explains the similar energy.

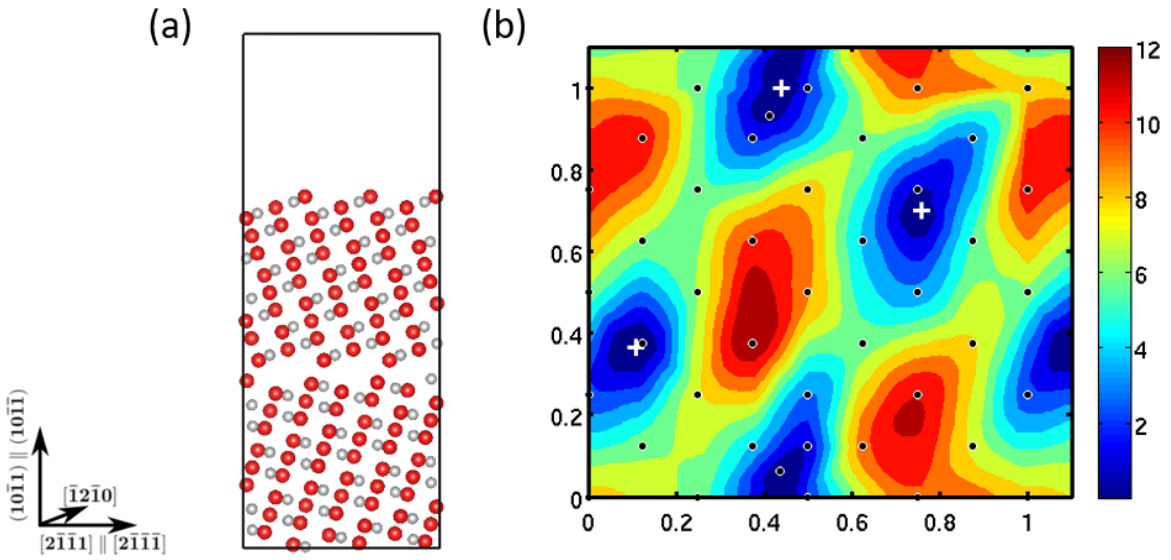

Figure 10 Alumina Σ11{$\mathbf{10\bar{1}1}$}/{$\mathbf{10\bar{1}\bar{1}}$} a) (0,0) structure where red balls correspond to O and gray to Al. b) adjusted 1x1 energy contour map. Minima are marked with white crosses while grid points and additional points are shown with black points.

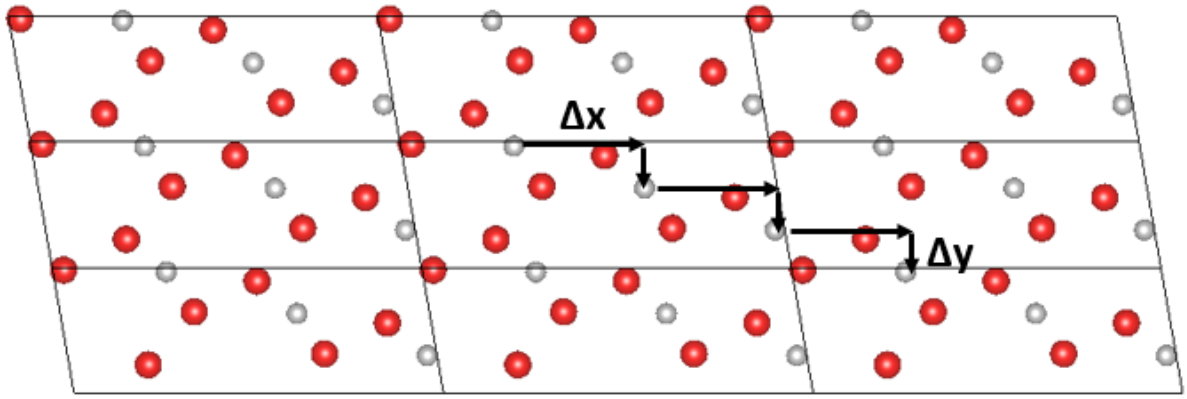

Figure 11 Shift in atomic positions from minima to minima, indicated by arrow path. Gray balls are Al and red balls are O.

Once the minima were determined for a fixed atomic distance, the separation distance was varied for the minima locations to determine the ideal separation distance between the two layers. When changing to a fully relaxed structure, there is an energy change of about- 7.5eV, as shown

in Table 8. This lower energy indicates the minima prefer to have a smaller separation distance than the initial 1Å. For the z-relaxed alumina $\Sigma 11\{10\bar{1}1\}/\{10\overline{1\bar{1}}\}$ grain boundary, all three minima have the same energy (with a variation ~0.05eV) when separation is fixed to 1Å. When full (x-, y-, and z-coordinates) relaxation occurs there is a larger deviation (~0.15eV), although all minima are found to have a 0.9Å separation distance.

Table 8 Energy (eV) and shortest separation distance (Å) for O and Al across the grain boundary for Al_2O_3 for both the fully relaxed, 0.9Å, case and the fixed 1Å separation.

	Z-relax (1.0Å)			Full relax (0.9Å)		
	(0.44, 1.00)	(0.76, 0.70)	(1.108, 0.365)	(0.44, 1.00)	(0.76, 0.70)	(1.108, 0.365)
Energy (eV)	-1301.72	-1301.72	-1301.77	-1309.21	-1309.30	-1309.15
Al-Al (Å)	2.588	2.698	2.638	2.626	2.645	2.635
Al-O (Å)	1.822	1.838	1.827	1.789	1.819	1.787
O-O(Å)	2.539	2.421	2.472	2.405	2.435	2.435

The difference between separation distance for Al-Al, Al-O, and O-O across the grain boundary can be seen in Table 8, and the structures in Figure 11. There does not seem to be a pattern to if the distance increases or decreases between the two relaxations, however the full relaxation has more shorter separation distances, perhaps due to the decreased separation distance (0.1Å). There also does not seem to be any correlation to which minima contains the shortest bonds

as it is different between the relaxation methods, however (0.44, 1.00) possesses four of the six shortest separation distances.

Figure 11 shows the structure for the fully relaxed 0.9Å grain boundary, Al are numbered to help show how the top grain is shifted in comparison to the bottom grain. A close inspection between atoms interacting with Al 1, 2, and 3 are different for each system, however their positions are nearly identical between each system. For example, for atom 1, in the (0.44, 1) grain boundary atom 6 in the closest, however for (0.76, 0.70) and (0.108, 0.365) Al 5 and 4 are closer, respectively, yet all three Al sit in the same position as explained in Figure 10.

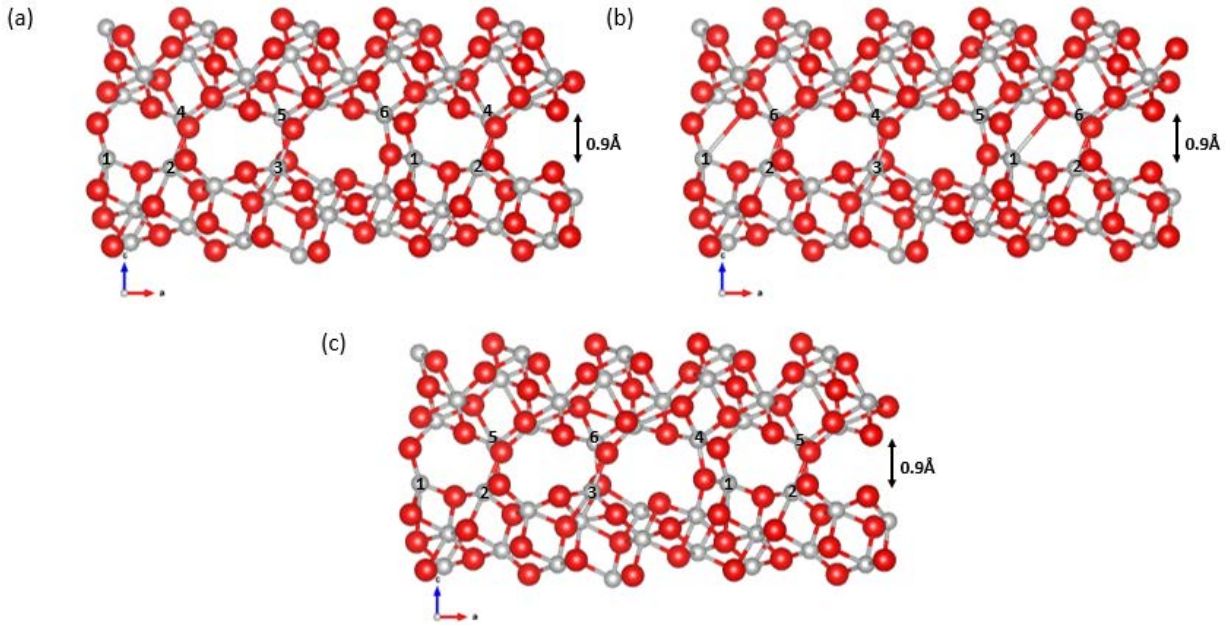

Figure 12 Grain boundary structure for fully relaxed undoped grain boundary a) (0.44, 1) b) (0.76, 0.7) and c) (0.108, 0.365), where red balls corresponds to O and gray balls to Al. Aluminum atoms are numbered to show how atoms have transitioned for each point in comparison to the bottom grain. The a-axis is $[\mathbf{2\bar{1}\bar{1}1}]||[\mathbf{2\bar{1}\bar{1}\bar{1}}]$ and c-axis is $(\mathbf{10\bar{1}1})||(\mathbf{10\bar{1}\bar{1}})$.

4.1.2 $\Sigma 11\{10\bar{1}1\}/\{10\bar{1}\bar{1}\}$ Alumina grain boundary doped with 1Y

First, Y doped $\Sigma 11\{10\bar{1}1\}/\{10\bar{1}\bar{1}\}$ is examined due to its popularity as a dopant in alumina. As previously stated, Y atoms replace Al on the grain boundary, a single Y on the grain boundary results in a breaking of the symmetry of the two grains, as seen in Figure 12a. The energy contour plot can be seen in Figure 12b (same scale as the undoped case). 1Y concentrations on the grain boundary does not result in a change in local minima locations, however there is a change in relative energy through the system. In comparison between the undoped (~12.25eV) system, the

energy variation between the highest energy point and the lowest energy point is smaller (~10eV), resulting in the more green and blue areas.

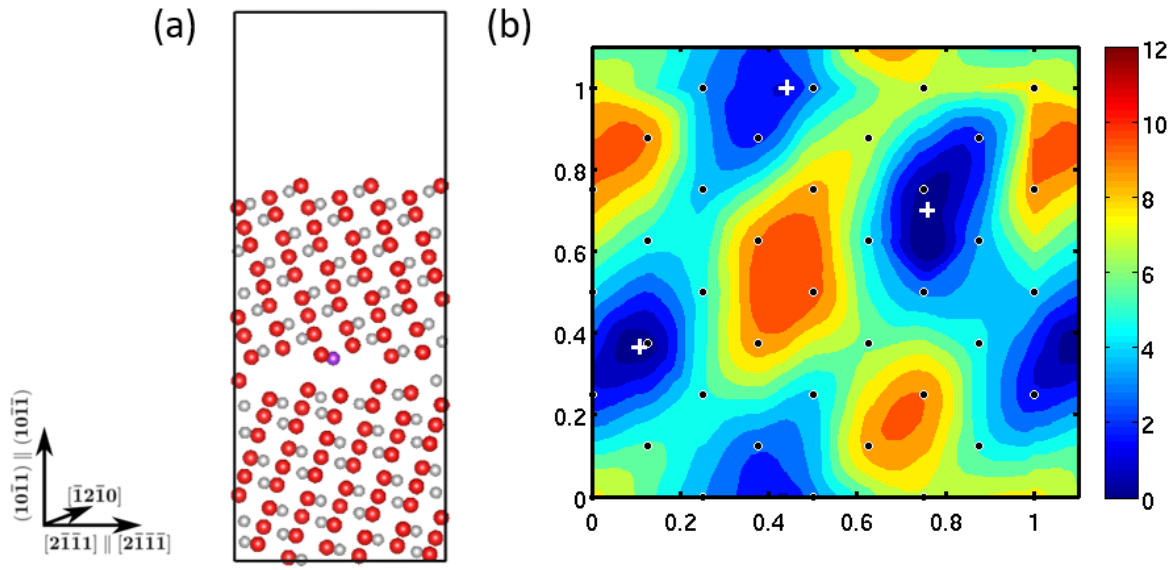

Figure 13 1Y on the grain boundary a) (0,0) structure where the Y atom is purple, Al is gray and red is O. b) adjusted 1x1 energy contour map. Minima are marked with white crosses while grid points and additional points are shown with black points.

Unlike the undoped system, two of the minima are similar in energy (0.13eV difference for (0.76, 0.7) and (1.108, 0.365)) and one has a higher energy (1.54eV difference for (0.44, 1)). Per thermodynamics the structure is more likely to be found in either minima of similar energy, however, the (0.44, 1) minima the structure is less likely to be found in that configuration due to the higher energy. This indicates including a single yttrium atom breaks the symmetry of the

minima structures of $\Sigma 11\{10\bar{1}1\}/\{10\overline{1\bar{1}}\}$ and would introduce a small amount of pinning, as one of the minima is no longer favorable.

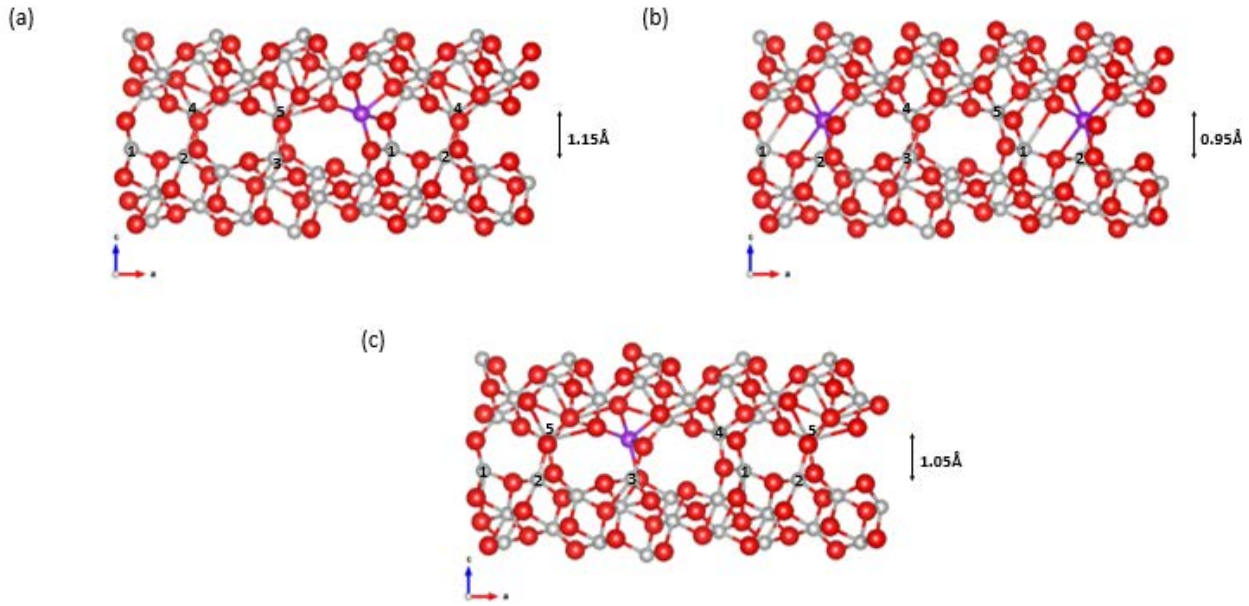

Figure 14 Grain boundary structure for fully relaxed a) (0.44, 1) b) (0.76, 0.7) and c) (0.108, 0.365), where red balls correspond to O, gray to Al, and purple to Y. Aluminum atoms are numbered to show how atoms have transitioned for each point in comparison to the bottom grain. The a-axis is $[\mathbf{2\bar{1}\bar{1}1}]||[\mathbf{2\bar{1}\bar{1}\bar{1}}]$ and c-axis is $(\mathbf{10\bar{1}1})||(\mathbf{10\overline{1\bar{1}}})$.

Upon full relaxation, it was found that unlike the undoped alumina grain boundary, the minima preferred different separation distances from each other, as well as from the undoped case; this can be shown in Figure 8 and separation distances across the grain boundary can be seen in Table 9. It was found that for the lowest energy minima, (0.76, 0.7), the separation was found to be 0.95Å, for (1.108, 0.365) separation was 1.05Å, and for the highest energy minima, (0.44, 1.0), the separation was 1.15Å. This indicates the larger distance between the two grains decreases the

probability of finding the grain boundary in the configuration. It is important to note that although the separation distances vary by 0.2Å between the fully relaxed structures, the atomic separation across the grain boundary does not change much between the different structures.

From Table 9 it is observed that Y-O bonds across the boundary all decrease upon full relaxation, except for Y-O for (1.108, 0.365) which remains the same distance, even though the distance between grains changes. Full relaxation also increases the bond length of all Y-Al separation distances, however the bond lengths for Al-Al, Al-O, and O-O do not have a pattern on increasing or decreasing upon fill atomic relaxation. Compared to the undoped case, most separation distances across the grain boundary increase when adding 1Y atom to the system.

Table 9 Energy (eV) and shortest separation distance (Å) for O and Al across the grain boundary for a single Y in Al_2O_3 for both the fixed 1Å separation and the fully relaxed case.

	Z-relax (1.0Å)			Full relax		
	(0.44, 1.00)	(0.76, 0.70)	(1.108, 0.365)	(0.44, 1.00) 1.15Å	(0.76, 0.70) 0.95Å	(1.108, 0.365) 1.05Å
Energy (eV)	-1302.35	-1303.90	-1303.77	-1312.58	-1312.91	-1312.77
Al-Al (Å)	2.80	2.72	2.65	2.77	2.69	2.67
Al-O (Å)	1.84	1.87	1.86	2.40	1.84	1.84
O-O (Å)	2.56	2.45	2.53	1.80	2.42	2.73
Y-Al (Å)	2.69	3.03	2.88	3.10	3.26	3.01
Y-O (Å)	2.12	2.10	2.20	2.09	2.09	2.20

4.1.3 $\Sigma 11\{10\bar{1}1\}/\{10\bar{1}\bar{1}\}$ Alumina grain boundary doped with 1Hf

Figure 14 shows the grain boundary doped with a single Hf atom, structure and energy contour plot with the same scale as the undoped case. As with Y, the introduction of a single Hf atom does not change the locations of the local maxima and minima. However, compared to the undoped case, there are more points with higher energy, indicated by the increase in amount of red and orange, and none of the minima are equivalent, as indicated by the different shades of blue at the minima. For a single Hf atom, the (0.76, 0.7) minima has the lowest energy, with (1.108, 0.365) and (0.44, 1.0) having energies approximately 1 and 2eV higher respectively. This further increases the amount of pinning compared to Y, as only one minima is preferred via thermodynamics.

Structural analysis was again performed on the local minima for the fixed 1Å separation as well as the fully relaxed structures. The fully relaxed structures for each of these minima can be seen in Figure 15 and separation distances can be seen in Table 10. Between the 1Å separation distance and the fully relaxed structures, the Hf-Al bond distance changed the most (~0.2Å), and Hf-O changed the least (~0Å). For all minima, the distance between the Hf atom and the closest Al atom increased as the system fully relaxes. In comparison between the undoped case, there is a larger difference between the changes in Al-Al, Al-O, and O-O distances, however this change in bond length is not equivalent to the change in separation distance.

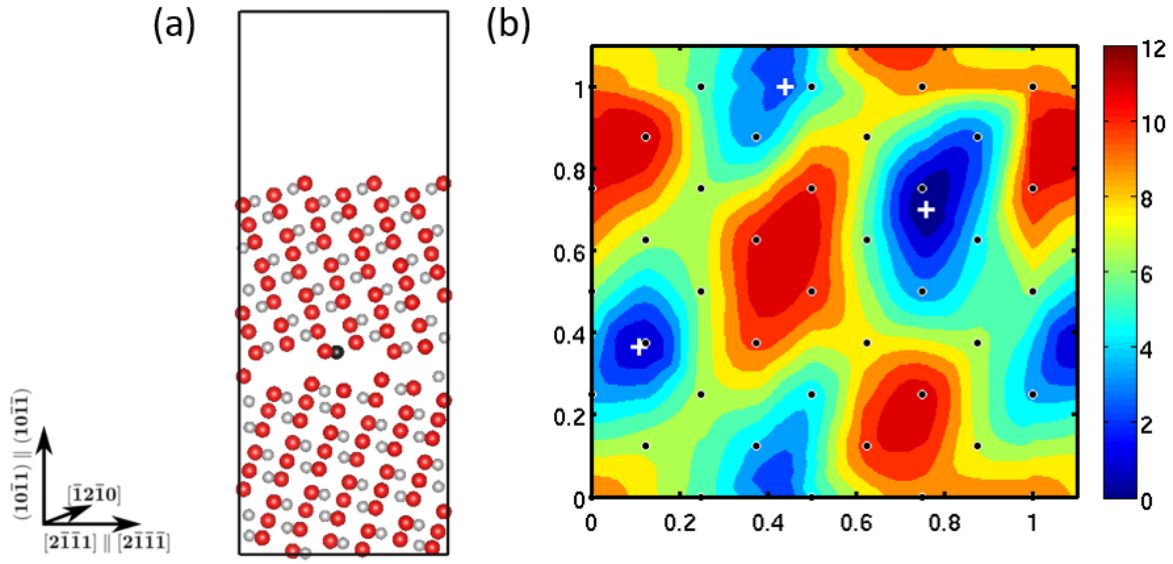

Figure 15 1Hf on the grain boundary a) (0,0) structure where the Hf atoms is black, Al is gray and red is O. b) adjusted 1x1 energy contour map. Minima are marked with white crosses while grid points and additional points are shown with black points.

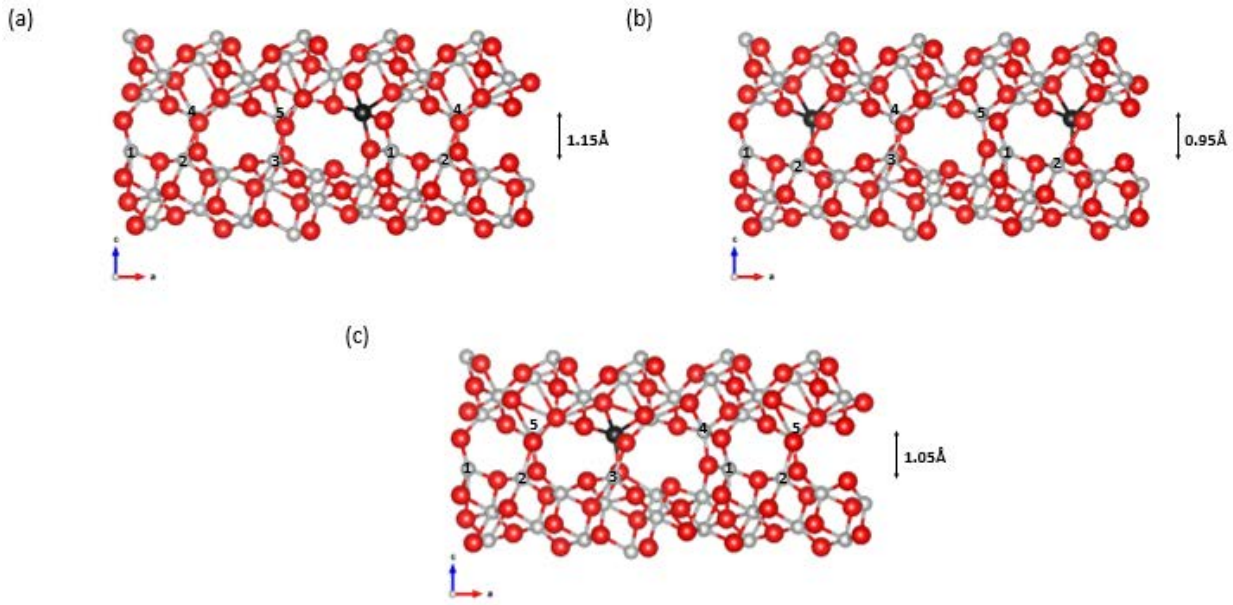

Figure 16 Grain boundary structure for fully relaxed a) (0.44, 1) b) (0.76, 0.7) and c) (0.108, 0.365), where red balls correspond to O, gray to Al, and black to Hf. Aluminum atoms are numbered to show how atoms have transitioned for each point in comparison to the bottom grain. The a-axis is $[\mathbf{2\bar{1}\bar{1}1}]||[\mathbf{2\bar{1}\bar{1}\bar{1}}]$ and c-axis is $(\mathbf{10\bar{1}1})||(\mathbf{10\bar{1}\bar{1}})$.

Table 10 Energy (eV) and shortest separation distance (Å) for O and Al across the grain boundary for a single Hf in Al_2O_3 for both the fixed 1Å separation and the fully relaxed case.

	Z-relax (1.0Å)			Full relax		
	(0.44, 1.00)	(0.76, 0.70)	(1.108, 0.365)	(0.44, 1.00) 1.15Å	(0.76, 0.70) 0.95Å	(1.108, 0.365) 1.05Å
Energy (eV)	-1307.02	-1309.78	-1308.72	-1315.46	-1316.08	-1315.52
Al-Al (Å)	2.76	2.76	2.65	2.75	2.66	2.64
Al-O (Å)	1.81	1.84	1.84	1.77	1.75	1.75
O-O (Å)	2.57	2.44	2.52	2.41	2.43	2.52
Hf-Al (Å)	2.66	2.98	2.86	2.86	3.07	2.94
Hf-O (Å)	1.99	1.95	2.06	1.99	1.964	2.02

In comparing the 1Y and 1Hf grain boundary systems, we observe the same separation distances for all three minima. However, the energy change between the z-relaxed and full relaxed systems is lower for the Hf case, approximately 9.4eV for Y and 7.2eV for Hf. It can also be noted in general the bond lengths across the grain boundary are shorter for 1Hf than the 1Y grain boundary, in particular, the Y atom all bond lengths across the boundary are longer than their Hf counterparts.

4.1.4 $\Sigma 11\{10\bar{1}1\}/\{10\overline{1\bar{1}}\}$ Alumina grain boundary doped with 2Hf

Due to the larger change in $\Sigma 11\{10\bar{1}1\}/\{10\overline{1\bar{1}}\}$ alumina with Hf in comparison to Y, we then examined an alumina system with 2 Hf (~33% grain boundary coverage, 1.2at% doping for the complete simulation cell) on the grain boundaries, one on each side, as can be seen in Figure 18a below. The same simulations were then performed. It was found that the minima shifted slightly in position, however the difference was less than 0.05-fractional coordinates, thus we treated the minima as though they were in the same place. Examining the energy contour plot for 2Hf grain boundary, Figure 18b, there is a larger area of high energy compared to the 1Hf grain boundary, this results in a larger difference between the maxima and minima for 2Hf (~12.4 eV) in comparison to 1Hf (~11 eV) grain boundaries. For 2Hf there are again two minima with similar energy ((0.44, 1) and (1.108, 0.365) vary by 0.28eV), however, they are higher by the global minima ((0.76, 0.7)) by over 2.5eV. This shows the structure is even more favorable than the 1Y and Hf cases per thermodynamics, introducing an even greater amount of pinning.

Full atomic relaxation performed on the minima shows that the additional Hf atom did not result in a change in the ideal separation distances from the single doped grain boundary concentration systems. The structure of full relaxation can be seen in Figure 18, and the bond lengths across the grain boundary can be seen in Table 11. There is a larger amount of atomic relaxation when adding a second Hf atom (Figure 17), this can be seen by the change in atomic positions interacting with the bottom Hf atom.

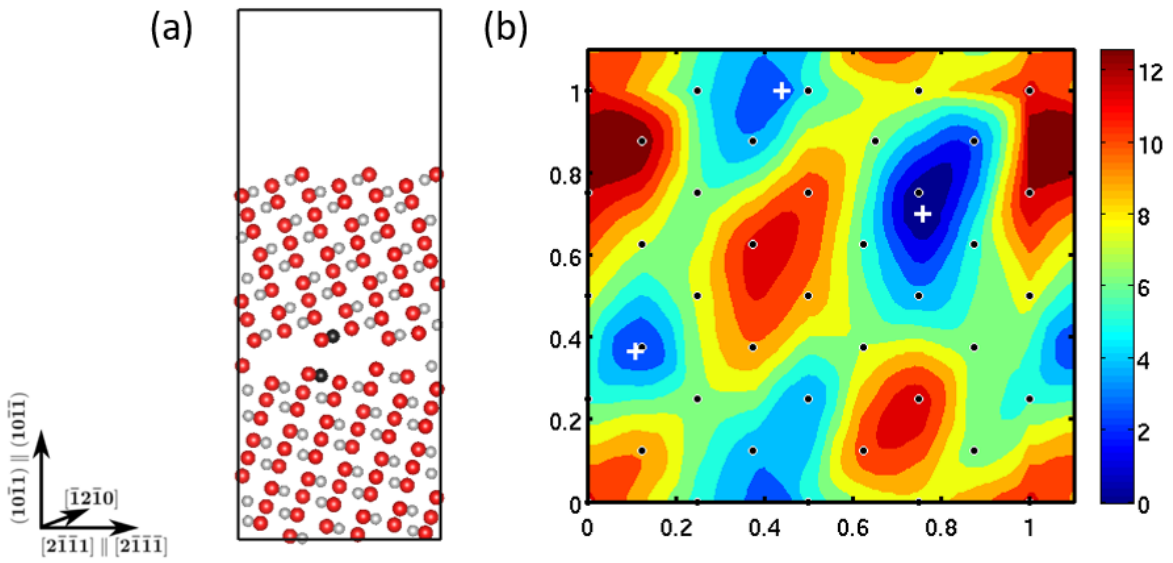

Figure 17 2Hf grain boundary a) (0,0) structure and b) adjusted 1x1 energy contour map. Minima are marked with white crosses while grid points are shown with black points.

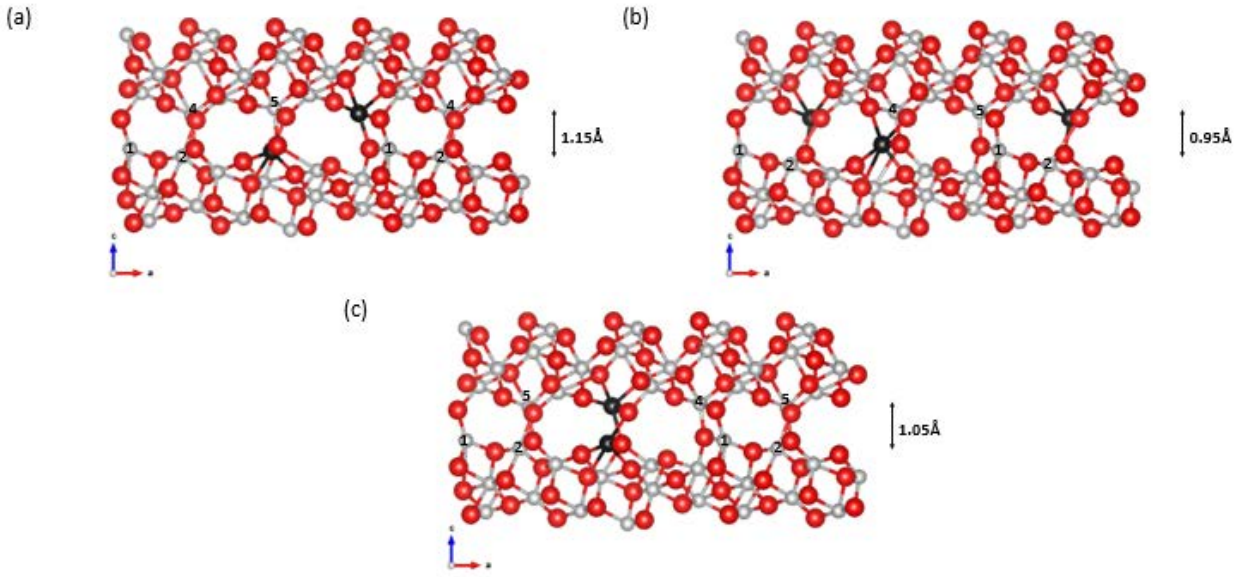

Figure 18 Grain boundary structure for fully relaxed a) (0.44, 1) b) (0.76, 0.7) and c) (0.108, 0.365), where red balls correspond to O, gray to Al, and black to Hf. Aluminum atoms are numbered to show how atoms have transitioned for each point in comparison to the bottom grain. The a-axis is $[\mathbf{2\bar{1}\bar{1}1}]||[\mathbf{2\bar{1}\bar{1}\bar{1}}]$ and c-axis is $(\mathbf{10\bar{1}1})||(\mathbf{10\bar{1}\bar{1}})$.

As can be seen in Table 11 the absolute minima, (0.76, 0.7), has the largest separation distance between the two Hf for a fixed separation distance of 1Å. However, there does not seem to be a direct correlation to distance between Hf atoms and energy, as (1.108, 0.365) has a shorter separation distance and lower energy than (0.44, 1). For the fixed separation distance, comparing the undoped and 2Hf grain boundary cases, Al-O separation distances are shorter for 2Hf grain boundary, however Al-Al and Al-O are longer. Compared to the grain boundary with 1Hf, there does not appear to be a pattern on bond distances increasing or decreasing, however ~56% of bonds are longer for 2Hf.

Table 11 Energy (eV) and shortest separation distance (Å) for O and Al across the grain boundary for a two Hf in Al_2O_3 for both the fixed 1Å separation and the fully relaxed case.

	Z-relax (1.0Å)			Full relax		
	(0.44, 1.00)	(0.76, 0.70)	(1.108, 0.365)	(0.44, 1.00) 1.15Å	(0.76, 0.70) 0.95Å	(1.108, 0.365) 1.05Å
Energy (eV)	-1313.77	-1316.65	-1314.05	-1320.94	-1322.40	-1321.65
Al-Al (Å)	3.04	2.71	2.65	2.86	2.64	2.63
Al-O (Å)	1.82	1.84	1.84	1.80	1.81	1.80
O-O (Å)	2.57	2.56	2.49	2.4	2.67	3.10
Hf-Al (Å)	2.65	2.69	5.77	2.82	3.25	5.40
Hf-O (Å)	1.99	1.95	2.19	1.97	1.97	2.06
Hf-Hf (Å)	5.68	5.95	2.70	5.09	6.33	2.97

4.1.5 Effects of Doping on Σ11{$10\bar{1}1$}/{$10\bar{1}\bar{1}$} Alumina

Introducing dopants into the grain boundary results in a structural and electronic change as indicated in Table 12 below. Both Y and Hf ions are larger than Al, by ~68 and ~46% respectively, typically believed to result in site-blocking [19]. Y has the same number of valence electrons as Al, however Hf increases the number of electrons by 1, which may result in the swamping-out mechanic suggested by Nakawaga [19]. Y and Al have the same number of valence electrons, which indicates there should be no charge effects and only size should affect the grain boundary. For Hf, however, there is an increase in ion size as well as a decrease in charge, which may affect both swamping out and site-blocking mechanisms.

Table 12 Ion volume and valence electrons for Al, Y, and Hf.

Element	Ion radius (Å)	Charge	Valence electrons
Al	0.535 [81]	3+	$3s^2p^1$
Y	0.90 [82]	3+	$4d^1\ 5s^2$
Hf	0.78 [83]	4+	$5d^6\ 6s^2$

To better understand the differences of the grain boundaries, one can examine the grain boundary energy, plotted in Figure 18, using Equations 2-4 and 2-5. For the grain boundary with 1Y, the grain boundary energy increases compared to the undoped grain boundary, indicating that a single Y in the grain boundary destabilizes the grain boundary. Adding one Hf to the grain boundary increases the stability, comparing to both the undoped and 1Y grain boundaries, as seen

by the decrease in formation energy. Adding a second Hf results in a further decrease in grain boundary formation energy, further stabilizing the structure.

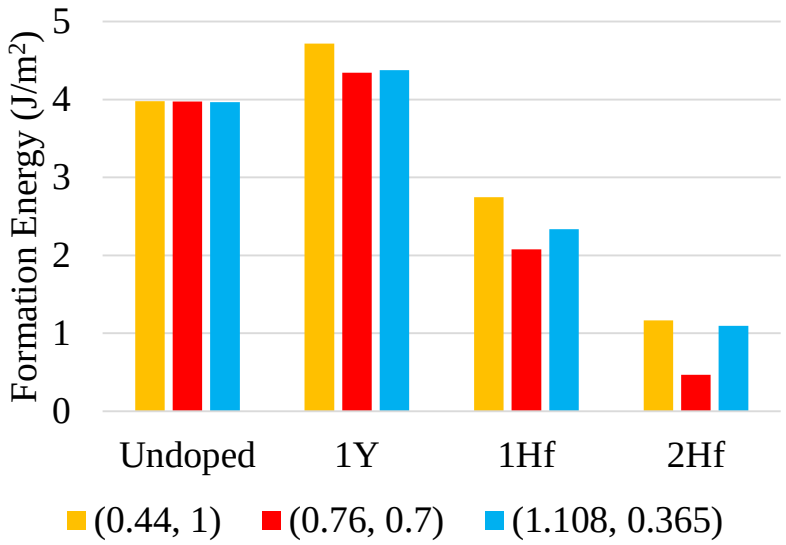

Figure 19 Grain boundary energy for the undoped surface and doped Σ11{$\mathbf{10\bar{1}1}$}/{$\mathbf{10\bar{1}\bar{1}}$} for the three minima.

Figure 18 again shows the minima for the undoped case have equal probabilities, shown by having the same grain boundary formation energy. In comparing the doped cases, it is observed that the (0.44, 0) minima contains the highest grain boundary energy for all three grain boundary configurations, indicating it is the least stable of the minima. However, the most stable grain boundary configuration is determined to be the (0.76, 0.7) grain boundary, indicated by the lower formation energy.

Due to the stability of the (0.76, 0.7) grain boundary, further analysis on the electronic structure was performed only for this minimum. The DOS for the 90 atoms closest to the grain boundary (to ensure some bulk properties and no surface effects) can be seen below in Figure 19,

where filled regions indicate the state is filled. It is important to note the bulk (also 90 atoms) DOS contains a different scale in the y-direction, reaching to 110 instead of 60. All four grain boundaries fill the valence band, however the defect states shown in the band gap are empty. The change in the structure results in a change in DOS shape and states are filled beyond the Fermi energy of bulk alumina, indicating the grain boundary becomes an electron/hole conductor where diffusion can occur more rapidly [33].

1Y grain boundary introduces small changes to the states near the valence band maximum, as well as increases the number of states in the conduction band. The addition of a single Hf results in the defect states appearing within the band gap, at 3.6eV. There is also a change in number of states in the valence band, as indicated by the bulge at approximately 0.25 eV. Adding a second Hf atom results in defect states appearing even closer to the valence band, at ~2.8 eV. The states near the valence band also experience a change in shape, introducing a sharp peak near 0.14 eV and a more rapid decrease in the number of states beyond the peak.

The DOS is commonly referred to as an arbitrary unit, however comparing the value of the DOS at zero electron energy for each grain boundary may provide insight to the change in diffusion behavior. These values are approximately 28.25, 35, 30 and 27 for the undoped, 1Y, 1Hf, and 2Hf cases respectively. 1Y and Hf in the grain boundary increases in value, indicating additional holes near the valence band in which diffusion can occur. The opposite is true for the 2Hf grain boundary, where a decrease is observed, indicating a reduced number of holes near the valence band.

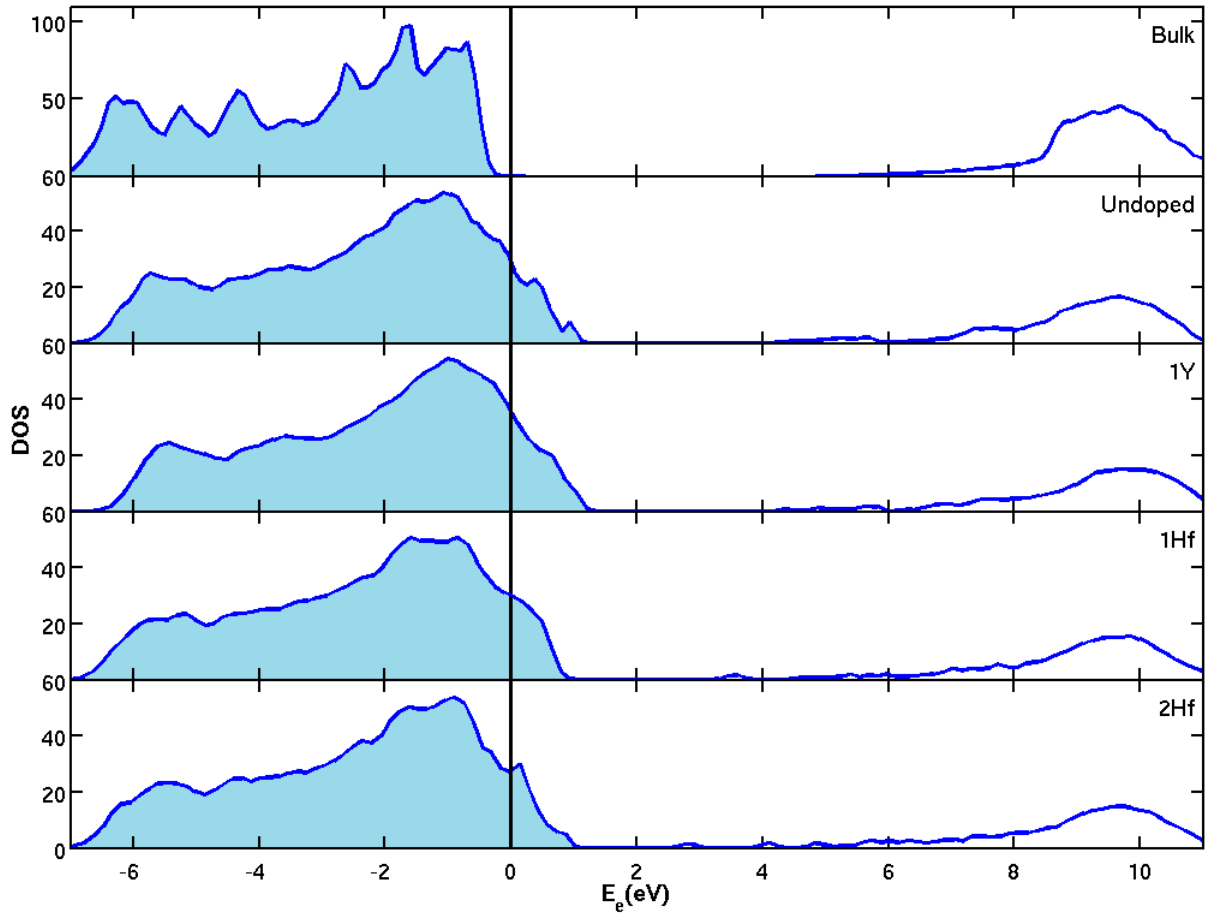

Figure 20 Partial density of states for bulk alumina and the undoped, 1Y, 1Hf, and 2Hf $\Sigma 11\{\mathbf{10\bar{1}1}\}/\{\mathbf{10\bar{1}\bar{1}}\}$ grain boundary for the (0.76, 0.7) minima. The shaded regions indicate filled states.

Charge density was also examined for the (0.76, 0.7) minima to explain some differences observed in the DOS and grain boundary. Figure 20 shows the charge density for the undoped alumina $\Sigma 11\{10\bar{1}1\}/\{10\bar{1}\bar{1}\}$ grain boundary, here the increase in charge is observed by blue (surrounding the red oxygen atoms) and a decrease in charge density is blue (surrounding the gray aluminum atoms). The shape of the charge density around Al, Figure 20b, shows

directionality. And examining the local charge density of the Al atom, Figure 20c, shows a lack of charge density on the Al atom itself.

Replacing the Al atom in Figure 20 with Y and Hf can be seen in Figure 21 and Figure 22, respectively. Examining the Y charge density, the shape of the charge density is different than the Al it replaced, however it remains directional, Figure 21b. The Y atom also shows an increased charge density close to the atom, this can further be observed in Figure 21c. The three nodes of increased charge density lie within a plane, approximately 120° apart, and are approximately the same size, which is indicative of sp^2 hybridization [84]. Examining the partial DOS for the Y atom, Figure 21d, shows some overlap of the s- and p-orbitals. The lack of overlap of the p_z- and s-orbitals indicate indeed there is sp^2 hybridization.

Replacing Al with Hf results in a loss of directionality, Figure 22b. Hf also shows three nodes with increased charge density, Figure 22b, unlike Y, these nodes are not planar and angled like that of an sp^3 hybrid orbital. For Hf, however, there is not a fourth node present, as with sp^3 hybridized orbitals. Investigating the pDOS, there was no indication of hybridization, and becomes a point of future investigation.

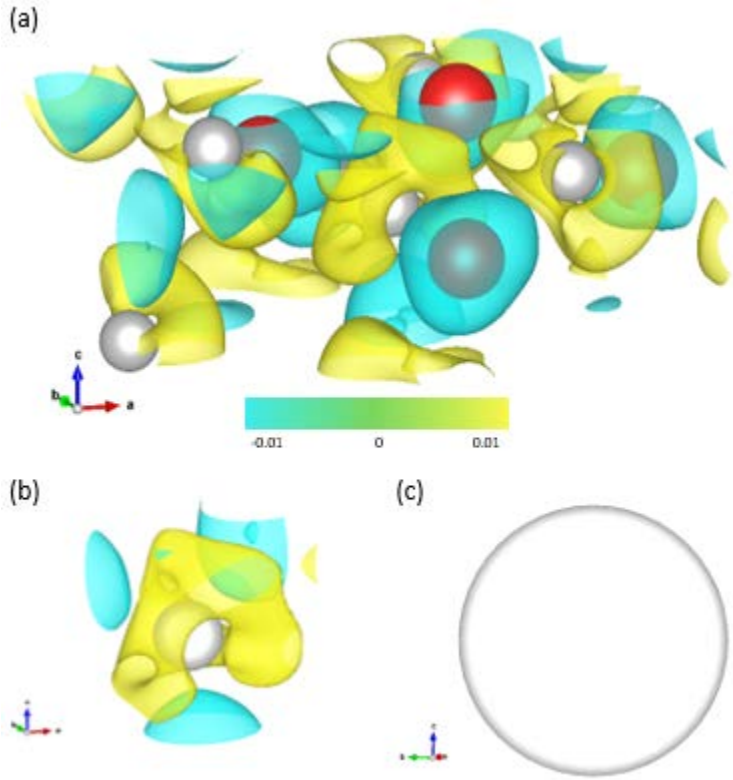

Figure 21 Charge density alumina Σ11{$\mathbf{10\bar{1}1}$}/{$\mathbf{10\bar{1}\bar{1}}$} a) area surrounding Al atom in the grain boundary b) only the Al atom in the grain boundary and c) only the negative isosurface for the Al atom. Where the a-axis is [$\mathbf{2\bar{1}\bar{1}1}$]||[$\mathbf{2\bar{1}1\bar{1}}$], the b-axis is [$\mathbf{\bar{1}2\bar{1}0}$], and c-axis is ($\mathbf{10\bar{1}1}$)||($\mathbf{10\bar{1}\bar{1}}$); and red balls are O and gray are Al.

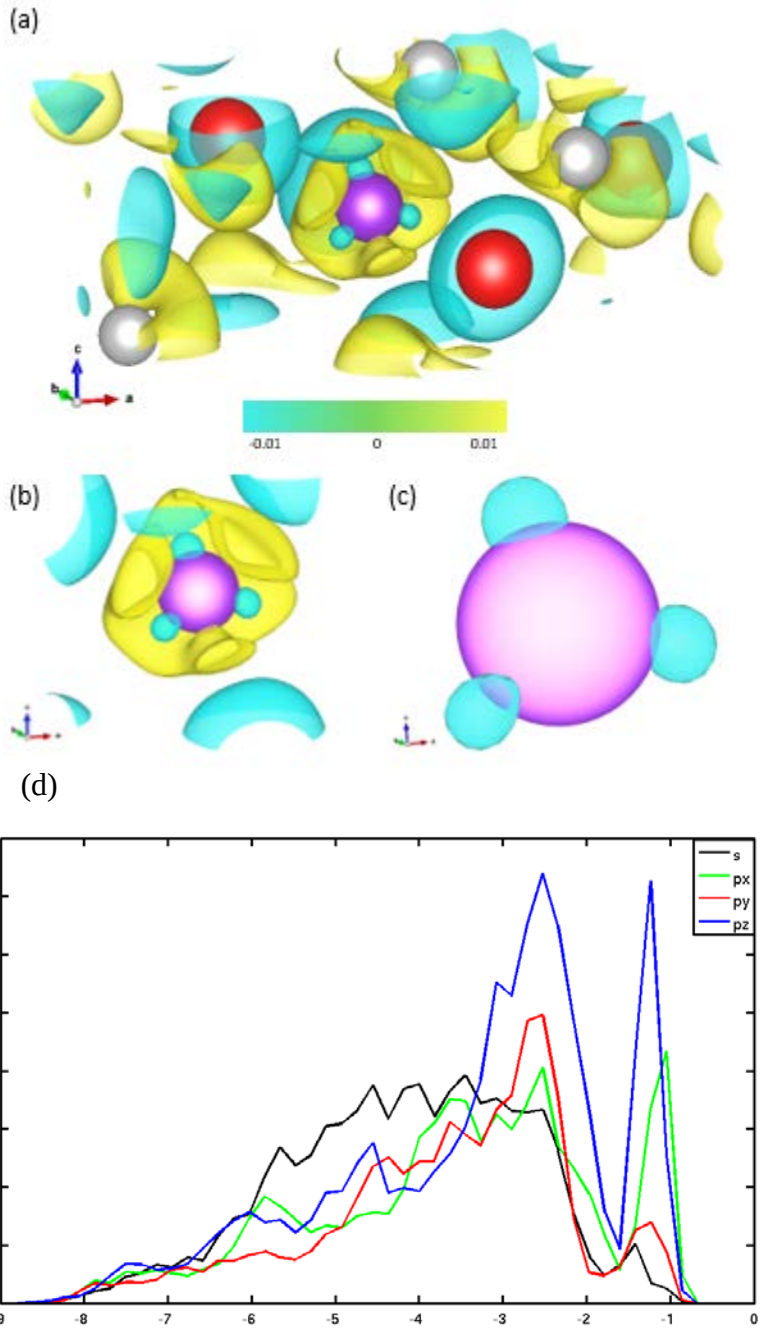

Figure 22 Charge density for 1 Y Σ11{$\mathbf{10\bar{1}1}$}/{$\mathbf{10\bar{1}\bar{1}}$} a) area surrounding Y atom in the grain boundary b) only the Y atom in the grain boundary and c) only the negative isosurface for the Y atom. Where the a-axis is [$\mathbf{2\bar{1}\bar{1}1}$]||[$\mathbf{2\bar{1}1\bar{1}}$], the b-axis is [$\mathbf{\bar{1}2\bar{1}0}$], and c-axis is ($\mathbf{10\bar{1}1}$)||($\mathbf{10\bar{1}\bar{1}}$); and red balls are O, gray are Al, and purple is Y. d) Shows the partial DOS for the Y atom. Where black is the s-orbital, green is p_x, red is p_y, and blue is p_z.

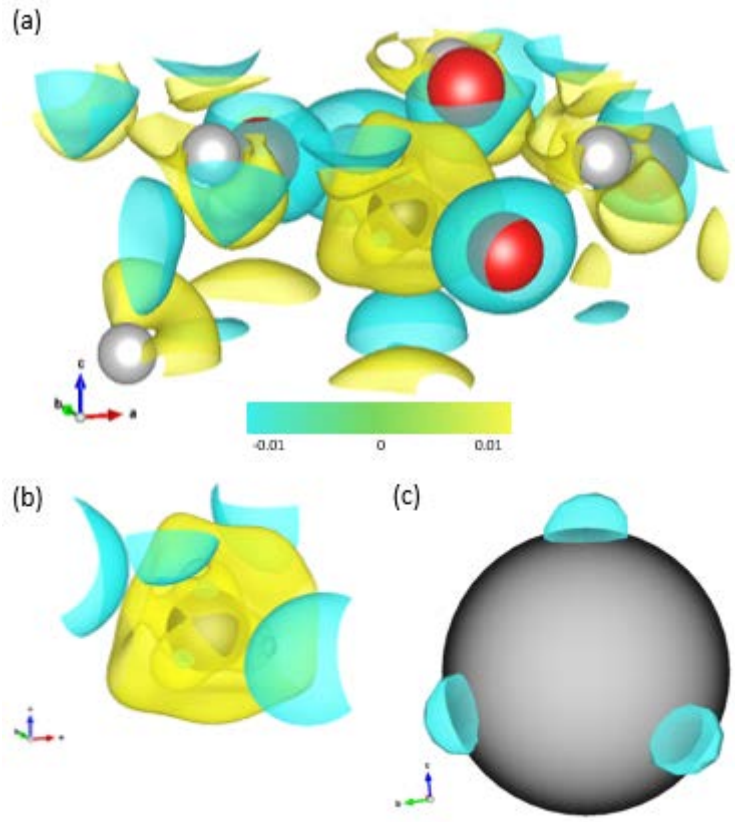

Figure 23 Charge density for 1 Hf Σ11{$\mathbf{10\bar{1}1}$}/{$\mathbf{10\bar{1}\bar{1}}$} a) area surrounding Hf atom in the grain boundary b) only the Hf atom in the grain boundary and c) only the negative isosurface for the Hf atom. Where the a-axis is [$\mathbf{2\bar{1}\bar{1}1}$]||[$\mathbf{2\bar{1}1\bar{1}}$], the b-axis is [$\mathbf{\bar{1}2\bar{1}0}$], and c-axis is ($\mathbf{10\bar{1}1}$)||($\mathbf{10\bar{1}\bar{1}}$); and red balls are O, gray are Al, and black is Hf.

4.2 DISCUSSION

The changes in relative energy of the minima with respect to each other and the change in DOS helps explain the changes grain boundary diffusion behavior for $\Sigma 11\{10\bar{1}1\}/\{10\overline{\bar{1}1}\}$ when doped with Hf and Y. In comparing the global minima, (0.76, 0.7), there is an increase in the ideal separation distance between the undoped and doped cases. For the undoped case, a free volume of ~60.5Å^3 is contained within the grain boundary. When doping with both Hf and Y, the free volume increases to ~63.9 Å^3, indicating a larger separation distance is needed when larger atoms are present in the grain boundary. This increase in free volume is normally indicative of increased diffusion [22], however there are many effects one must consider.

The introduction of 1Y in the grain boundary makes it such that two of three minima are of nearly equal probability, slowing grain-boundary diffusion by introducing some pinning. Instead, when 1Hf is added to the grain boundary, the minima become even more separated in terms of relative stability, where a global minimum is formed and more pinning is introduced. The pinning introduced due to thermodynamic stabilities effectively would slow grain boundary diffusion.

The charge density shows the remarkably different bonding properties for the three metals in the same position in the grain boundary. Al and Y show directional bonding where Hf shows non-directional bonding. There also is a difference in the local charge density, indicating a different behavior of the bonds. For Al and Hf no hybridization is observed. However, for Y the 5s and 4p atomic orbitals hybridize into an sp^2 orbital, Figure 21c and Figure 21d. These changes in bonding result in increased bond distance for the metal to the O across the grain boundary during full atomic relaxation for both Hf and Al. Our results show that Y bonds are longer than their Hf counterparts, indicates a more rapid diffusion process due to bond strength, in agreement with Milas *et al*. [20].

One must also consider the increased number of states near the valence band indicates an increased number of holes while the number of states near the conduction band maximum influences the number of holes; which in turn alters the diffusion of ions through the grain boundary [33, 41]. For 1Y and 1Hf, there is an increase number of states increases near the valence band maximum, indicating more holes for diffusion which in turn influences Al/O diffusion within the grain boundary. However, there is an increase in the number of defect states introduced in the band gap for 1Hf. These defect states allow for electrons to diffuse through the grain boundary easier, and allow for more opportunities for annihilation of electrons and holes, and thus slowing their diffusion in the band gap. The introduction of more pinning and the increased probability of annihilation of electrons and holes results in a decreased diffusion through the grain boundary. This effect is observed to be stronger for 1Hf than 1Y in the grain boundary, in agreement with previous results which showed a slowing of mass gain [21] and stronger M-O bond strengths [20] when using Hf.

Experimentally, concentrations of up to 0.5% are added to alumina to reduce oxidation, where approximately 0.2 of a monolayer has been observed within the grain boundary [85]. However, we find further increasing the concentration of Hf in the grain boundary to 2Hf (1/3 monolayer) increases the amount of pinning by further enhancing the stability of the global minima compared to 1Hf. Unlike both single-atom doped grain boundaries, 2Hf reduces the number of states when the near the valence band maximum, indicating a reduced number of holes. There are also defect states deeper within the band gap, indicating electrons may diffuse even easier. The combination of less holes and more electrons may provide an increased amount of annihilation, slowing diffusion even further.

4.3 CONCLUSIONS

Doping Y and Hf to the $\Sigma 11\{10\bar{1}1\}/\{10\overline{11}\}$ alumina grain boundary shows a change in electronic properties and stability of configurations of the grain boundary. 1Y in the grain boundary shows small changes in grain boundary behavior, indicating a small decrease in diffusion. 1Hf in the grain boundary is shown to have a greater effect on slowing diffusion than Y, due to pinning and shorter bond lengths. Increasing the concentration of Hf to two atoms in the grain boundary, the changes in diffusion become more pronounced, indicating concentration has a large effect on grain boundary diffusion in the $\Sigma 11\{10\bar{1}1\}/\{10\overline{11}\}$ alumina.

4.4 FUTURE WORK

The research performed here examines the effects of Hf and Y at two concentrations (17% and 33%) on the structure of a $\Sigma 11\{10\bar{1}1\}/\{10\overline{11}\}$ alumina grain boundary. From the change in energy contour maps (Figure 14b and Figure 16b) and DOS (Figure 19) we can see there is a dependence on the concentration on the behavior in the grain boundary. In the future testing a higher concentration may be examined, however one must proceed with caution, as adding more, larger ions may result in unstable atomic configurations at 1Å separation distance.

Heuer *et al.* suggest that the change in accessibility of electrons and holes by Y is an important factor for improving polycrystaine performance, in particular, oxygen permutation [37]. Now that global minima positions have been found, examining the effects of Y and Hf in the grain boundary on a more classical point defect jumping view of diffusion can provide further insight to how reactive elements change the diffusion properties of alumina grain boundaries. Figure 23

shows a possible oxygen vacancy path one can consider when examining diffusion in the grain boundary.

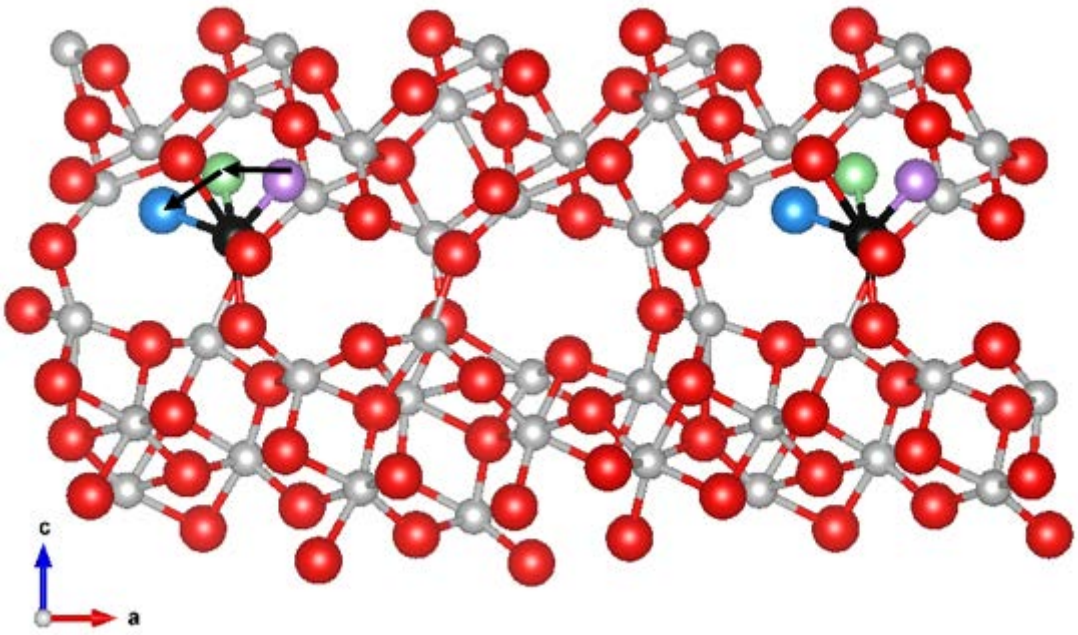

Figure 24 Example diffusion path for an oxygen vacancy diffusion in a 1Hf concentration in Σ11{$\mathbf{10\bar{1}1}$}/{$\mathbf{10\bar{1}\bar{1}}$}. Red balls are O, gray are Al, and black is Hf; blue, green, and purple show possible positions for the oxygen vacancy.

5.0 THESIS CONCLUSIONS

For this work, we set out to examine the electronic effects on diffusion in the lattice and grain boundary. For lattice diffusion, charged and neutral charged vacancies were examined using DFT and DFT+U methods. It was found that vacancy diffusion is strongly influenced by its charge, we observed a neutral Cr and O vacancy has a larger migration energy in comparison to the charged vacancies ($V_{\mathrm{O}}^{2+}\ and\ V_{\mathrm{Cr}}^{3-}$). It was also observed that during migration, the defect states in the DOS changed depending on the position of the vacancy, effecting the migration energy. Doped (1Y, 1Hf, and 2Hf) and undoped alumina grain boundaries were examined, and it was found that doping the $\Sigma 11\{10\bar{1}1\}/\{10\overline{\bar{1}1}\}$ grain boundary results in a change in stabilities of geometric structures. While changes were observed for 1Y and 1Hf electronic properties, reaching a critical point, in this case 2Hf, results in a change in the DOS near the conduction band maximum resulting in a slowing of grain boundary diffusion.

BIBLIOGRAPHY

1. E. Celik, C. Tekmen, I. Ozdemir, H. Cetinel, Y. Karakas, S.C. Okumus, Surf. Coat. Technol. **174** (2003) 1074.

2. P.F. Tortorelli. J. Phys. IV **3** (1993) 943.

3. P. Kofstad, K.P. Lillerud, J. Electrochem. Soc. 127 (1980) 2410.

4. M. Nastasi, D.M. Parkin, and H. Gleiter. "Mechanical Properties and Deformation Behavior of Materials Having Ultra-Fine Microstructures" Springer Science & Business Media 2012.

5. S.J. Schneider and C.L. McDaniel. J. Res. NBS A Phys. Ch. **71A** (1967) 317-333.

6. W.E. King and J.H. Park. J. Phys. Colloques **51** (1990) C1-555.

7. S. Hallstörm, M. Halvarsson, L. Höglund, T. Jonsson, and J. Ågren. Solid State Ionics, **240** 41 (2013).

8. S.M. Allen and E.L. Thomas, *The Structure of Materials*, WILEY (1999).

9. H .E. Evans, A.T. Donaldson, and T.C. Gilmour, Oxid. Met. **52** (1999) 379.

10. S.C. Tsai, A.M. Huntz, C. Dolin, Mater. Sci. Eng., A **212** (1996) 6–13.

11. S.C. Tsai, A.M. Huntz, C. Dolin, Oxid. Met. **43** (1995) 581-595.

12. S.C. Tsai, A.M. Huntz, and J. Philibert, Defect. Diffus. Fourm. **143-147** (1997) 1195-1200.

13. A.C.S, Sabioni, A.M. Huntz, J. Philibert, B. Lesage, and C. Monty. J. of Mat. Sci. **27** (1992) 4782-4790.

14. Y. Lei, Y. Gong, Z. Duan, and G. Wang. Phys. Rev. B **87** (2013) 214105-214117.

15. Y. Lei and G. Wang, Scripta. Mater. **101** (2015) 20.

16. H. Yu, C. Chen, R. Jiang, P. Qiu, and Y. Li. J. Phys. Chem. C, **116** (2012) 25478.

17. F. Lebreau, M.M. Islam, B. Diawara, and P. Marcus, J. Phys. Chem. C **118** (2014) 18133-18145.

18. D. Naumenko, B.A. Pint, and W.J. Quadkkers. Oxid. Met. **86** (2016) 1-43.

19. T. Nakagawa, I. Sakaguchi, N. Shibata, K. Matsunaga, T. Mizoguchi, T. Yamamoto, H. Haneda, Y. Ikuhara. Acta. Mater. **55** (2007) 6627-6633.

20. I. Milas, B. Hinnemann, E.A. Carter. J. of Mater. Chem. **21** (2011) 1447-1456.

21. I. Rommerskirchen and V. Kolarik. Matter and Corros. **47** (1996) 625-630.

22. A.H. Heuer, T. Nakawaga, M.Z. Azar, D.B. Hovis, J.L. Smialek, B. Gleeson, N.D.M Hine, H. Guhl, H.-S. Lee, P. Tangney, W.M.C. Foulkes, M.W. Finnis. Acta. Mater. **61** (2013) 6670-6683.

23. Z.G. Yang, D.M. Paxton, K.S. Weil, J.W. Stevenson, and P. Singh. Tech. Rep. PNNL-14116, U.S. Department of Energy under Contract DE-AC06-76RL01830, 2002.

24. A.H. Heuer. J. Euro. Ceram. Soc. **28** (2008) 1495-1507.

25. J. Cho, H.M. Chan, M. P. Harmer, and J.M. Rickman. J. Am. Ceram. Soc. **81** (1998) 3001-3004.

26. P. Lejček. Springer Ser. Mater. S. **136** (2010) 5-24.

27. T. Nakagawa, H. Nishimura, I. Skaguchi, N. Shibata, K. Matsunaga, T. Yamamoto, and Y. Ikuhara. Scripta. Mater. **65** (2011) 544-547.

28. T. Gemming, S. Nufer, W. Kurtz, and M. Rühle. J. Am. Ceram. Soc. **86** (2003) 581-589.

29. Y. Ikuhara, H. Nishimura, A. Nakamura, K. Matsunaga, T. Yamamoto, and K.P.D. Lagerlöf. J. Am. Ceram. Soc. **86** (2003) 595–602.

30. H. Nishimura, K. Matsunaga, T. Saito, T. Yamamoto, and Y. Ikuhara. J. Am. Ceram. Soc. **86** (2003) 574-580.

31. A.G. Marinopoulos, S. Nufer, and C. Elsässer. Phys. Rev. B. **63** (2001) 165112.

32. S. Fabris, S. Nufer, C. Elsässer, T. Gemming. Phys. Rev. B **66** (2002) 155415.

33. H. Guhl, H-S Lee, P. Tangney, W.M.C. Foulkes, A.H. Heuer, T. Nakagawa, Y. Ikuhara, and M.W. Finnis. Acta. Mater. **99** (2015) 16-28.

34. S. Fabris and C. Elsässer. Phys. Rev. B **64** (2001) 245117.

35. S. Fabris and C. Elsässer. Acta. Mater. **51** (2003) 71-86.

36. H. Yoshida, Y. Ikuhara, T. Sakuma. J. Mater. Res. **13** (1998) 2597-2601.

37. A.H. Heuer, D.B. Hovis, J.L. Smialek, B. Gleeson. J. Am. Ceram. Soc. **94** (2011) 146-153.

38. Z. Yu, Q. Wu, J. M. Rickman, H. M. Chan, and M.P. Harmer. Scripta. Mater. **68** (2013) 703-706.

39. J. Chen, Y.-N. Xu, P. Rulis, L. Ouyang, and W.-Y. Ching. Acta. Mater. **53** (2005) 403-410.

40. I. Milas, B. Hinnemann, E.A. Carter. J. Mater. Res. **23** (2008) 1494-1508.

41. A.H. Heuer, M.Z. Azar, H. Guhl, M. Foulkes, B. Gleeson, T. Nakagawa, Y. Ikuhara, and M.W. Finnis. J. Am. Chem. Soc. **99** (2016) 733-747.

42. M. Le Gall, A.M Huntz, B. Lesange, C. Monty, J. Bernardini. J. of Mat. Sci. **30** (1995) 201-211.

43. T. Höche, P.R. Kenway, H-J Kleebe, M. Ruhle, and P.A. Morris. J. Am. Ceram. Soc. **77** (1994) 339.

44. P.R. Kenway. J. Am. Ceram. Soc. **77** (1994) 349.

45. H. Müllejans and R.H. French. J. Phys. D: Appl. Phys. **29** (1996) 1751-1760.

46. S.-D. Mo, W.-Y. Ching, and R.H. French. J. Am. Ceram. Soc. **79** (1996) 627-633.

47. I. Milas and E.A. Carter. J. Mater. Sci. **44 (**2009) 1741-1749.

48. J.P. Hirth. J. Phys. Chem. Solids **55** (1994) 985-989.

49. A.H. Heuer and M.Z. Azar. Scripta. Mater. **102** (2015) 15-18.

50. B. Gleeson. Personal contact.

51. A.H. Heuer. J. Euro. Ceram. Soc. **28** (2008) 1495-1507.

52. G. Kresse and J. Hafner, Phys. Rev. B **47** (1993) 558.

53. G. Kresse and J. Furthmüller. Comput. Mater. Sci. **6**, (1996) 15.

54. G. Kresse and D. Joubert. Phys. Rev. B **59** (1999) 1758.

55. J. P. Perdew, K. Burke, and M. Ernzerhof. Phys. Rev. Lett. **77** (1996) 3865.

56. P. Hohenberg and W. Khon. Phys. Rev. **136** (1964) B864-B871.

57. W. Khon and L.J. Sham. Phys. Rev. **140** (1965) A1133-1138.

58. M. Born and R. Oppenheimer. Zur Quantentheorie der Molekeln **389** (1927) 457-484.

59. D.R. Hartree. Math. Proc. Camb. Philos. Soc. **24** (1928) 89–132; 426–437.

60. V. Fock. Z. Phys. **61** (1930) 126-148.

61. A.I. Liechtenstein, V.I. Anisimov, J. Zaanen. Phys. Rev. B **52** (1995) R5467.

62. Y. Wang, H. Fang, C. L. Zacherl, Z. Mei, S. Shang, L. Chen, P. D. Jablonski, Z. Liu. Surf. Sci. **606** (2012) 1422.

63. G. Henkelman, B. P. Uberuaga, and H. J´onsson. J. Chem. Phys. **113**, (2000) 9901.

64. G. Makov and M. C. Payne. Phys. Rev. B **51** (1995) 4014.

65. D. R. Renneke and D. W. Lynch. Phys. Rev. **138** (1964) A530.

66. M. W. Finnis, A. Y. Lozovoi and A. Alavi, Annu. Rev. Mater. Res., **35** (2005) 167.

67. R. C. Weast, ed., CRC Handbook of Chemistry and Physics, 69th Edition, CRC Press, Inc (1988-1989).

68. C. Gray, Y. Lei, and G. Wang. J. Appl. Phys. **120** (2016) 215101.

69. R.H. Bruce and D.S. Cannell. Phys. Rev. B **15** (1977) 4451.

70. S. Shi, A.L. Wysocki, and K.D. Belashchenko. Phys. Rev. B, **79** (2009) 104404.

71. J. E. Jaffe, M. Dupuis, and M. Gutowski. Phys. Rev. B **69**, (2004) 205106.

72. L.W. Finger and R.M. Hazen. J. Appl. Phys. **51** (1980) 5362.

73. P.J. Brown, J.B. Forsyth, E. Lelièvre-Berna, and F. Tasset. J. Phys. -Condensed Mat. **14** (2002) 1957.

74. J.A. Crawford and R.W. Vest. J. Appl. Phys. **35** (1964) 2413.

75. A. Janotti, J. B. Varley, P. Rinke, N. Umezawa, G. Kresse, and C. G. Van de Walle, Phys. Rev. B **81** (2010) 085212.

76. S. Shi, Y. Qi, H. Li, and L.G. Hector, J. Phys. Chem. C **117** (2013) 8579.

77. A.C.S. Sabioni, A.M. Huntz, F. Millot, and C. Monty, Philos. Mag. A **66** (1992) 351.

78. A.C.S. Sabioni, B. Lesage, A.M. Huntz, J.C. Pivin, and C. Monty, Philos. Mag. A **66** (1992) 333.

79. K.J.W. Atkinson, R.W. Grimes, M.R. Levy, Z.L. Coull, T. English. J. Eur. Ceram. Soc. **23** (2003) 3059-3070.

80. A.A. Sokol, A. Walsh, C.R.A. Catlow. Chem. Phys. Let. **492** (2010) 44-48.

81. E. Gaudry, D. Cabaret, P. Sainctavit, C. Brouder, F. Mauri, J. Goulon and A. Rogalev. J. Phys.: Condens. Matter **17** (2005) 5467–5480.

82. T. T. Van, J.R. Bargar, and J.P. Chang. J. Appl. Phys. **100** (2006) 023115.

83. X. Zhao and D. Vanderbilt. Phys. Rev. B **65** (2002) 233106.

84. A. Ricca and C.W. Bauschlicher Jr. Chem. Phys. **200** (1995) 337-345.

85. P.Y. Hou. J. Am. Ceram. Soc. **86** (2003) 660-668.